Università Cattolica del Sacro Cuore
Sede di Brescia

Facoltà di Scienze Matematiche, Fisiche e Naturali
Corso di Laurea specialistica in Fisica


# Time-resolved optical spectroscopy of $CuGeO_3$

Tesi di Laurea

Damiano Nardi
Matricola n. 3208624

Relatore: Ch.mo Dott. Gabriele Ferrini
Correlatore: Ch.mo Prof. Fulvio Parmigiani

Anno Accademico 2005/2006

# Contents

# Chapter 1

# Introduction

## 1.1 Overview

Time-resolved optical spectroscopy is among the leading techniques to study important topics such as ultrafast solid-solid phase transitions and strongly correlated systems. In recent years the advent of ultrashort coherent pulses allowed to investigate solid-state physics in the femtosecond timescale. At present, shorter excitation pulses, to investigate electronic processes occurring on the attosecond timescale, and higher probing photon energies, to study ultrafast structural dynamics, represent the frontiers of this research field.

In particular, the excitation of solid systems by means of ultrashort pulses plays a fundamental role in the study of novel materials or not yet well explained mechanisms. Light pulses can be used to induce electronic and structural phase transitions in molecular crystals or in compounds classified as strongly correlated systems, being their properties dominated by strong electron correlation effects. The investigation of the physical mechanisms, responsible for the solid-solid ultrafast transitions and for the relaxation dynamics that follows, is mandatory to understand the electronic and optical properties of these materials.

The aim of this thesis is to investigate the electronic properties of $CuGeO_3$, upon strong excitation with ultrashort light pulses. This study is performed through femtosecond time-resolved optical spectroscopy. Copper germanate is a strongly correlated system and it was discovered to be the first inorganic compound exhibiting a particular magneto-elastic transition known as spin-Peierls, under a critical temperature of about 14 K. This transition occurs in a system of linear antiferromagnetic Heisenberg chains coupled to three dimensional phonons. It leads to a deformation of the magnetic lattice and to a structural transition, with the opening of a gap in the spectrum of magnons. Standard band calculations predict a metallic state for this cuprate, however it has an insulating character due to the strong electron correlations. These facts have led to intensive experimental investigation of its physical properties. In the past, the optical, electronic and magnetic properties and the origin of the spin-Peierls transition have been studied in pure and substituted $CuGeO_3$ crystals. Quite recently, optical and X-ray spectroscopy studies have been realized to reach a more detailed understanding of both the electron correlation mechanisms and the electronic and magnetic structure of this compound. The investigation of pure and substituted copper germanate have been performed in an extended temperature range, and a series of important spectral features has emerged. Structures detected in the range 1.4-2.3 eV have been attributed to phonon assisted *d-d* transitions, while another feature, detected for the electric field parallel to the crystal *c* axis at about 3.2 eV, has been ascribed to the formation of a particular type of exciton, made up of one electron and two neighboring holes in a singlet state, classified as Zhang-Rice exciton.

In this thesis, we study two aspects of the material's optical properties:

- As preliminary measurements, we investigate the linearity of the optical absorption. We separately study the pump beam absorption and the probe beam absorption, as a function of the incident radiation intensity on the sample.

- We perform time-resolved transmittivity variation measurements. Through a pump and probe technique, we study the effects of the photo-excitation of the Zhang-Rice excitons in the sample on the absorption dynamics in the *d-d* transitions energy region at 1.57 eV. The measurements are carried out in the four possible linear polarization orientations of the pump and the probe beams with respect to the crystal axes. For each configuration, we perform a series of measurements varying the pump incident power.

## 1.2 Outline

This work consists of two main sections.

The first section is constituted by Chapters 2 and 3. In Chapter 2 we present the crystal structure of the compound and its electronic configuration, we report a description of $CuGeO_3$ strong electron correlation mechanism, we give a brief overview of the spin-Peierls transition it undergoes.

In Chapter 3 we present a resume of the recent results in the analysis of the $CuGeO_3$ absorption spectrum (Fig. 3.1). Our attention is focused on the weak absorption band at 1.7 eV ascribed to phonon assisted *d-d* transitions and on the recently detected structure at 3.2 eV attributed to the formation of a Zhang-Rice exciton.

The second section is developed in Chapters 4, 5 and 6. In Chapter 4 we introduce our time-resolved optical absorption measurements. We give a description of the pump and probe technique adopted, specifying our needs in terms of pump incident intensity for the photo-excitation of the doping in the sample.

The experimental set-up developed for time-resolved optical spectroscopy measurements is described in Chapter 5, in both the configurations for non-linear absorption and time-resolved transmittivity variation investigations.

In Chapter 6 we present and discuss the results from the time-resolved transmittivity variation measurements. We show that the $CuGeO_3$ non-linear absorp-

tion of the pump radiation does not influence the measurements. The time-resolved measurements, in the four possible linear polarization orientations of the pump and probe beams with respect to the crystal axes, are analyzed varying the pump incident power. The excitation and relaxation dynamics are discussed.
In this way we give a starting point for a deeper time-resolved investigation aimed at clarifying the physical mechanisms responsible for the $CuGeO_3$ optical absorption.

# Chapter 2

# Strong electron correlation properties of $CuGeO_3$

Standard band calculations predict a metallic state for the cuprate $CuGeO_3$, however the compound has an insulating character due to the strong electron correlation. This is the case when the on-site electron-electron repulsion arising from Coulomb and exchange interactions is much greater than the one-electron dispersional band width. Therefore in narrow band systems like this, involving well-localized $3d$ electrons, the Coulomb repulsion overcomes the kinetic energy of the electrons, thus suppressing the charge fluctuations necessary for metallic conduction.

In this section we present the crystal structure of the compound and its electronic configuration, we report a description of $CuGeO_3$ strong electron correlation mechanism and we give a brief overview of the spin-Peierls transition it undergoes.

## 2.1 Crystal structure of $CuGeO_3$

In most of the copper oxide based materials the relevant structural unit is a plaquette made up of a Cu ion coordinated with four oxygens in a square planar

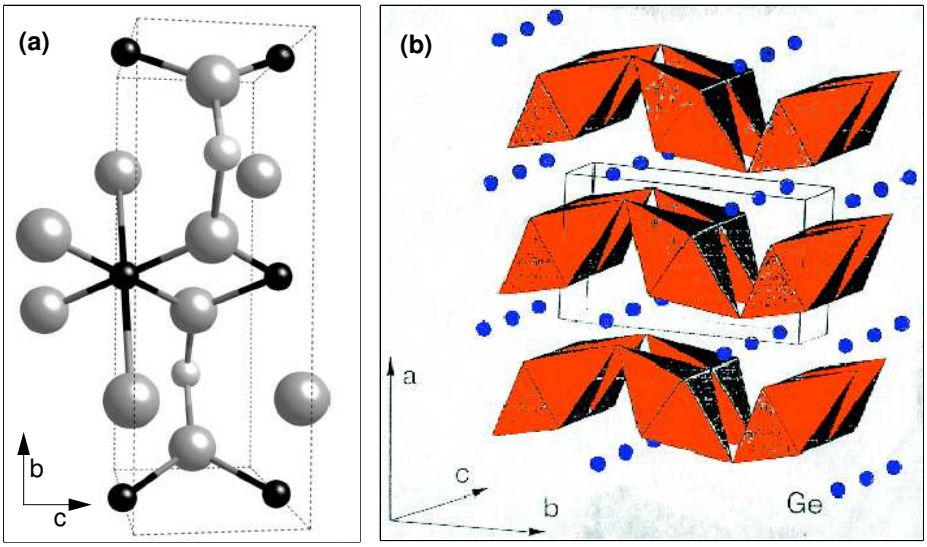


FIGURE 2.1: Crystal structure of $CuGeO_3$. (a) Dark spheres represent Cu ions, large light spheres O ions and small light spheres Ge ions. For one of the Cu ions the sixfold coordination is shown [3]. (b) The building blocks of the crystal structure are edge sharing $CuO_6$ octahedra and corner sharing $GeO_4$ tetrahedra stacked along the $c$ direction [4].

configuration. $CuGeO_3$ has an orthorhombic unit cell crystal structure. At room temperature the lattice parameters are $a$=4.81 Å, $b$=8.47 Å and $c$=2.94 Å. It belongs to the space group Pbmm (x//$a$, y//$b$, z//$c$) [1, 2]. The building blocks of the crystal structure are edge-sharing $CuO_6$ elongated octahedra and corner-sharing $GeO_4$ tetrahedra stacked along the $c$ direction (Fig. 2.1b).

The elongated octahedron is formed by a $Cu^{2+}$ ion at the center of a square of four $O^{2-}$ ions, and by the coordination of the same $Cu^{2+}$ ion with two apical O ions (Fig. 2.1a). We define O(1) the apical oxygen ions and O(2) the basal ions in the square coordination. Comparing the Cu-O bonds, the 2.76 Å Cu-O(1) distance to the apical oxygens is greater than the 1.94 Å Cu-O(2) distance to the basals. The edge sharing octahedra form chains with rather short Cu-Cu distances. The $CuO_6$ octahedra are quite distorted, with the Cu-O(1) bond not perpendicular to the basal plane accounting for two different O(1)-O(2) edge lengths (Fig. 2.2a). Cu

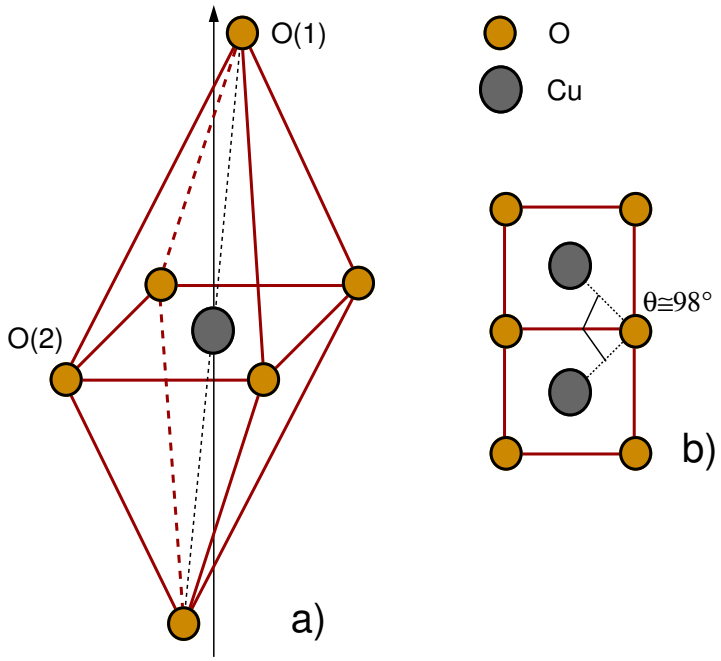


FIGURE 2.2: Crystal structure of $CuGeO_3$. (a) Distorted elongated octahedron. (b) $CuO_4$ plaquettes. The $98^0$ Cu-O(2)-Cu angle is shown.

ions connected by an O(2) pair bridge form antiferromagnetic (AF) linear chains along the crystal $c$ axis and the Cu-O(2)-Cu angle has been measured to be $\theta \simeq 98^0$ (Fig. 2.2b). The compound results to be antiferromagnetic, although the Cu-O-Cu angle is closer to $90^0$ than $180^0$. Thus, copper germanate seems to disagree with the Goodenough-Kanamori-Anderson rules stating that with a $90^0$ metal-oxygen-metal angle a ferromagnetic order is expected, whereas when the angle is $180^0$ the compound is antiferromagnetic [5, 6, 7]. An explanation can be given considering the presence of Ge attached to O ions influencing the AF superexchange character of the Cu-O(2) bond. The $GeO_4$ tetrahedra are almost perfect with quite equal Ge-O bond distances and O-O edges. The O-Ge-O angles are close to the ideal tetrahedral values and these structures are also chained together along one of their edges.

While the high temperature cuprate superconductors present a crystal structure completely filled by different type of cation-anion polyhedra, $CuGeO_3$ has

rather large empty cavities which are related to the presence of spontaneous giant strains along all three orthorhombic directions, as confirmed by high resolution thermal expansion measurements [2].

## 2.2 Electronic structure of $CuGeO_3$

In this section we describe the electronic structure of $CuGeO_3$. The single-atom electronic configurations for the composing elements are:

- O $\rightarrow 1s^2\ 2s^2\ 2p^4$
- Cu $\rightarrow 1s^2\ 2s^2\ 2p^6\ 3s^2\ 3d^{10}\ 4s^1$
- Ge $\rightarrow 1s^2\ 2s^2\ 2p^6\ 3s^2\ 3d^{10}\ 4s^2\ 4p^2$

By taking into account the ionicity of the bonds, the static electronic distribution can be schematized as:

$$Cu^{2+}Ge^{4+}O_3^{6-}$$

Two copper electrons and four germanium electrons are taken by the oxygen ligands to fill the 2p shell (O $2p^6$). The Ge ion is left with a completely filled $3d^{10}$ band. The Cu ion remains with an odd number of electrons in a not completely filled outermost shell (Cu $3d^9$), with the possibility to have charge fluctuations, which are necessary for metallic conduction. On this basis, elementary one-particle band theory calculations predict a metallic behavior for the transition metal compound. However, in this compound strong electron-electron interactions lead to strongly correlated motion of the electrons. The on-site electron-electron repulsion arising from Coulomb and exchange interactions is much greater than the one-electron dispersional band width. Therefore in this narrow band system with well-localized $3d$ electrons, the Coulomb repulsion overcomes the kinetic energy of the electrons, thus suppressing the charge fluctuations.

## 2.3 Strongly correlated system

In this section we present an overview of $CuGeO_3$ electronic properties, in relation to its state of strongly correlated system. We regard as a correlation effect every purely electronic phenomenon that cannot be treated with the independent-electron approximation, which for crystalline materials is the elementary band theory of solids. The band theory asserts that if the density of states at Fermi level $\rho(\epsilon_F)$ is vanishing, the material must have insulating properties and it must have an even number of electrons per unit cell, since a band with orbital degeneracy $n$ can hold $2n$ electrons per unit cell. Reversing the conditions, the statement fails even for an even number of electrons filling the valence band; an overlap between the valence and the conduction bands makes real the possibility to have $\rho(\epsilon_F) \neq 0$. On the other hand, for an odd number of electrons per unit cell the material must be a metal because the band is partially filled. However, $CuGeO_3$ is one of the several transition metal compounds that do not follow these general rules.

Mott exemplified the mechanism of strong electron correlation, by considering a crystal composed of hydrogen atoms [8]. He analyzed the tight binding picture of the band structure of Na, a solid with one atom per unit cell. All atomic levels give rise to bands, but only the $3s$ band reaches a sizable width. The deeper bands are completely filled, while the $3s$ band is half-filled with one atom per unit cell, giving Na its metallic state. Now consider a periodic array of widely separated Na atoms, at large enough distances the system is no longer a metal but an array of neutral Na atoms. The electron hopping process should take place in order to have electrical conduction. Electrons should propagate through the lattice, leading to charge fluctuations. In the electron hopping process, we must take in consideration the strong Coulomb repulsion between two electrons sharing the same atomic shell. A large energy investment is required, since the two electrons are confined within a short distance on the atomic orbital. The intra-atomic Coulomb energy $U$ represents the most important feature in a system of interacting electrons moving

in a narrow band. In the solid state, for sufficiently narrow band with a $U$ ranging between 1 and 10 eV, the metallic state charge fluctuations are suppressed by this intra-atomic Coulomb interaction and the charge transfer process asks for a lot of energy to happen. This represents the Mott transition from a metallic to an insulating state.

To describe this two opposing behaviors it is usual to introduce the Hubbard model [9]. In this view, the many-body Hamiltonian takes in consideration both the electrons kinetic energy from the hopping, which drives the metallic behavior accounting for the delocalization of the electrons into Bloch states, and the Coulomb repulsion that leads the transition to a Mott insulator:

$$H = -\sum_{\langle i,j\rangle,\sigma} t_{ij} c^{\dagger}_{\sigma,i} c_{\sigma,i} + \frac{U}{2} \sum_{i,\sigma} c^{\dagger}_{\sigma,i} c_{\sigma,i} c^{\dagger}_{\bar{\sigma},i} c_{\bar{\sigma},i} \tag{2.1}$$

where $t_{ij}$ is the matrix element describing the electron hopping between the nearest neighbor $i$ $j$ Hubbard sites, $c$ and $c^{\dagger}$ are the particle annihilation and creation operators. The first term of Eq. 2.1 give reason of the electrons' kinetic energy, while the second term describes the repulsion between electrons sharing the same orbital. Since for $U = 0$ no electron correlation is present and the system is metallic for any filling between one and two electrons for site, the relevant feature is the strong-coupling limit $U \gg t$. Under this condition double occupancy is not favorable and at the ground state there is one electron on each site. The system is thus insulating, even if the filling is only 1/2, because moving an electron from one site to another would cost the energy $U$.

Transition metal compounds, as $CuGeO_3$, are one of the most important class of strongly correlated systems. As stated, band theory assumes each electron to move in an average periodic potential of all other electrons but the experiments showed that strong electron-electron interactions lead to strongly correlated motion of the electrons. These correlation effects split the partially filled $d$ band into a set of either completely filled or empty Hubbard subbands, which result embedded into a sequence of wider bands derived from the Oxygen ligand $2p$ and the transition

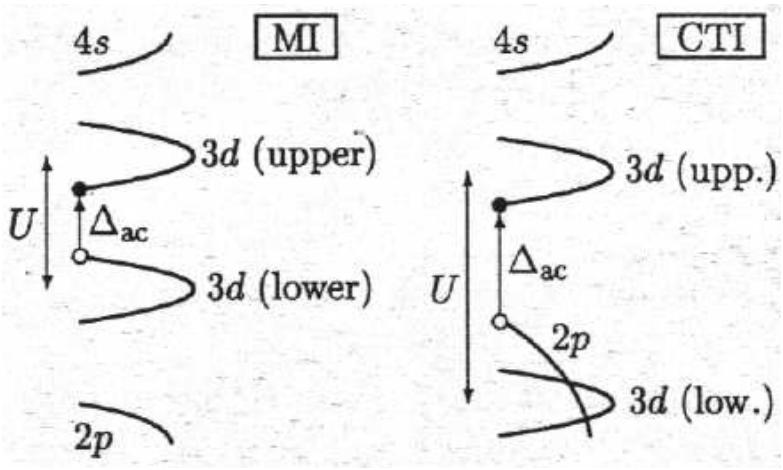


FIGURE 2.3: The character of the insulator is set by the lowest excitation energy $\Delta_{ac}$ sufficient to create a charge carrier. The shift of the relative positions of the Hubbard subbands and the $2p$ band give rise to different systems. The Mott insulator (MI) has the smallest gap between the two Hubbard subbands. $CuGeO_3$ is a charge transfer insulator system (CTI), where the lowest excitation involves an electron from the $2p$ band to the upper $3d$ subband [4].

metal $4s$ states, as shown in Fig. 2.3. The insulator characterization is given by the lowest excitation energy sufficient for creating a charge carrier [10]. The broadening of the levels into subbands happens when a $d$-like quasiparticle and a quasihole are created, thus able to propagate on the background of the $d$ ions with the $d$ electron kinetic energy. We assume that the $2p$ valence band and the lower Hubbard subband are completely filled. In the general Mott insulator (MI) the smallest gap is between the two Hubbard subbands and the lowest energy charge excitation $\Delta_{ac}$ is attributed to it. But the Mott-Hubbard gap is not necessarily the smallest gap. This is the case of copper germanate: a charge transfer insulator (CTI), where the most relevant excitation process removes an electron from the $2p$ ligand band placing it into the $3d$ upper Hubbard subband. In the excitation process a $d$-like quasiparticle and a $p$ hole are created and the conduction is hole-type, based on the higher mobility of 2p holes. The energy of the charge transfer

process $\Delta_{pd}$ is expressed by:

$$\Delta_{pd} = E_0\left(d^{n+1}\underline{L}\right) - E_0\left(d^n\right) \tag{2.2}$$

where $\underline{L}$ is the hole in the ligand band. The energy of the $d^n \rightarrow d^{n+1}\underline{L}$ process is lower than the *d-d* Coulomb repulsion $U_{dd}$. The activation energy $\Delta_{ac}$ is given by the CT process energy $\Delta_{pd}$ corrected with the terms $W_d$ and $W_p$ for the broadening of the quasiparticle and quasihole levels into subbands:

$$\Delta_{ac} = \Delta_{pd} - \frac{(W_d + W_p)}{2} \tag{2.3}$$

A classification diagram was proposed by Zaanen, Sawatzky and Allen [11] (Fig. 2.4), based on the relative values of $\Delta_{pd}$ and $U_{dd}$ and on the hybridization $t$ parameter of the metal to ligand transition. In this scheme the $CuGeO_3$ is classified as a charge transfer insulator, with a measured $O_{2p} \rightarrow Cu_{3d}$ energy smaller than the $U_{dd}$ Coulomb repulsion ($\approx$ 8-9 eV).

## 2.4 Spin-Peierls transition

Magnetic properties of low-dimensional systems of spins with antiferromagnetic (AF) interactions have attracted much attention because of various interesting phenomena, such as the spin-Peierls transition deforming the magnetic lattice in one-dimensional chains with alternating spin orientation and as the high-temperature superconductivity (HTSC) in layered cuprates including $CuO_2$ planes. Particular attention has been given to AF oxides containing $Cu^{2+}$ ions because of the responsibility of two dimensional $CuO_2$ planes for high-temperature superconductivity. The intensive experimental investigation of the various physical properties of copper germanate is started with the comparison of one dimensional $Cu^{2+}$ based antiferromagnets with 2D cuprate superconductors, but it experienced a burst after the discovery in 1993 for $CuGeO_3$ to be the first inorganic compound exhibiting a spin-Peierls (SP) transition [12].

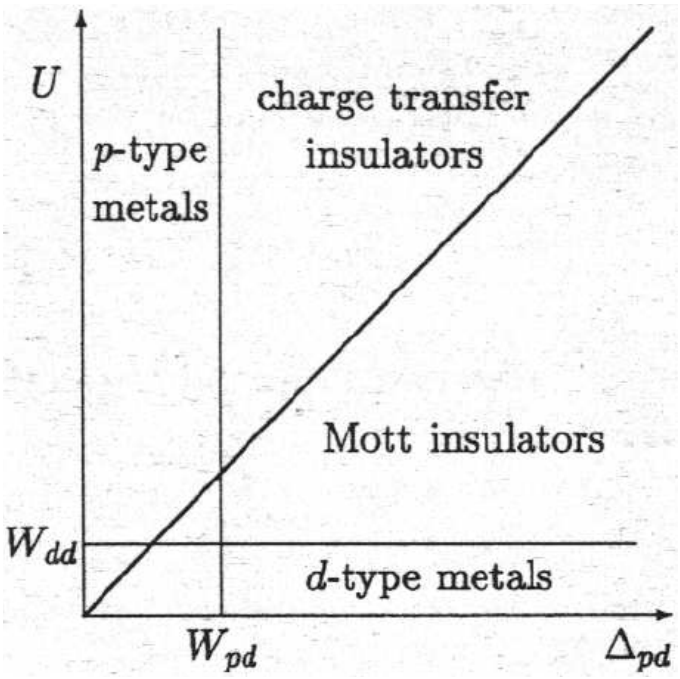


FIGURE 2.4: The Zaanen-Sawatzky-Allen diagram for the classification of strongly correlated insulators. If $U < \Delta_{pd}$ a Mott insulator (MI) is expected, whereas for $U > \Delta_{pd}$ as in our case, the compound is a charge transfer insulator (CTI). In general, when the hybridization increases the materials will go through an insulator-metal transition, obtaining $d$ or $p$ type metals [4].

This kind of magneto-elastic transition occurs in a system of linear Heisenberg antiferromagnetic chains coupled to three dimensional phonons. Under a certain critical temperature, this transition leads to a deformation of the magnetic lattice of the system. The interaction of the spin chain (period $a$) with the phonons brings up a sharp transition which modifies the chain in an alternating sequence of spins separated by a distance doubled (period $2a$), as shown in Fig. 2.5.

Peierls showed that the regular chain is unstable below a critical temperature [13, 14]. Through the transition the magnetic lattice constant doubles in value ($a \rightarrow 2a$), changing the size of the unit cell. This corresponds to have a Brillouin zone half as large in the spectrum of the magnons (reciprocal lattice) and to the creation of a magnetic gap (Fig. 2.6), with the lowering of the magnons' Fermi

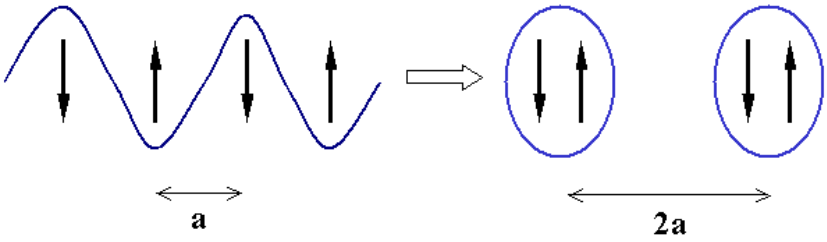


FIGURE 2.5: Spin-Peierls magnetic lattice deformation, due to the chain coupling to the three dimensional phonons.

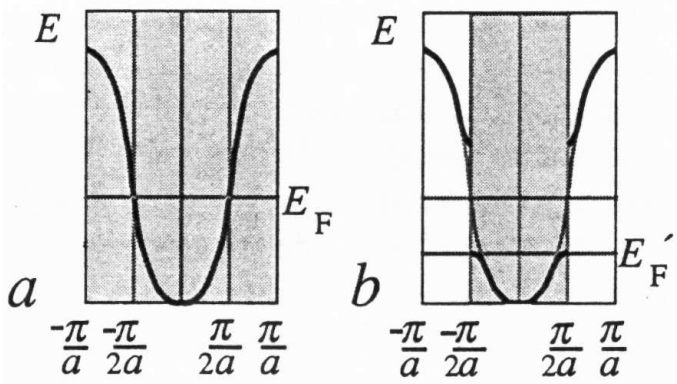


FIGURE 2.6: Band and Fermi energies for the regular linear chain (a) and the modified linear chain (b) of Fig. 2.5. The shaded areas indicate the first Brillouin zone corresponding to each case [14].

energy ($\Delta E_F$). On the other hand the potential energy is increased by the elastic energy of deformation ($\delta$), proportional to the spin displacement. The critical temperature for the transition is individuated when $\Delta E_F$ becomes of the order of $\delta$, and the modified chain results to be the stable phase. Above this point, the modified magnetic structure ceases to be stable and the spin-Peierls transition takes place in the system.

From Hase *et al.* [12, 15] to van Loosdrecht *et al.* [16, 17, 18], several experiments demonstrated without ambiguities the transition occurrence in $CuGeO_3$. The temperature dependence investigation showed an abrupt decrease of the magnetic susceptibility at about 14 K, with an energy gap in the magnons spectrum of 2.1 meV between a singlet ground state and the first excited state [12].

The traditional SP transition theory is based on one dimensional AF chain with nearest-neighbor magnetic coupling and a mean field handling of the three dimensional phonons. By those theoretical models describing a SP system in terms of a coupling between lattice and magnetic degrees of freedom, the presence of a phononic mode in the phonon spectrum, changing in intensity and in frequency upon going through the SP transition, is expected. However, optical techniques such as Raman and infrared spectroscopy, together with neutron scattering measurements have not yet unambiguously revealed this mode [19]. Moreover, most experiments on the magnetic properties of $CuGeO_3$ are better described by a 1D AF chain with alternating nearest-neighbor interactions together with an additional uniform next-near-neighbor magnetic exchange interaction, in spite of non-negligible interchain interactions.

The experimental measurements on substituted $CuGeO_3$ revealed a decrease of the spin-Peierls transition, not depending on the type of dopant. The Ge ions tetrahedrally coordinated with O linked to the chains have an important role in the SP transition, since the Si-substitution for Ge has proven to be more efficient in destroying the spin-Peierls phase, breaking the interaction between the Cu neighbors on chains adjacent to the Si ion [1].

# Chapter 3

# Optical absorption measurements of $CuGeO_3$

In this thesis we present a femtosecond time-resolved spectroscopic study of the optical absorption features of $CuGeO_3$, at room temperature. The compound's optical absorption spectrum is shown in Fig. 3.1. Recent experiments ascribed the weak absorption band at 1.7 eV to copper *d-d* transitions allowed by electron-phonon interactions [2, 3, 4]. The subsequent region of transparency is followed by a strong exponential edge identified with the onset of charge transfer transitions [2, 20]. Our attention is focused on a recently detected structure for the $\vec{E}$ field parallel to the *c* crystal axis at about 3.2 eV, which has been attributed to the formation of a Zhang-Rice (ZR) exciton [1]. This structure strongly depends on light polarization.

A resume of the analysis of the above $CuGeO_3$ optical absorption features is reported in this section.

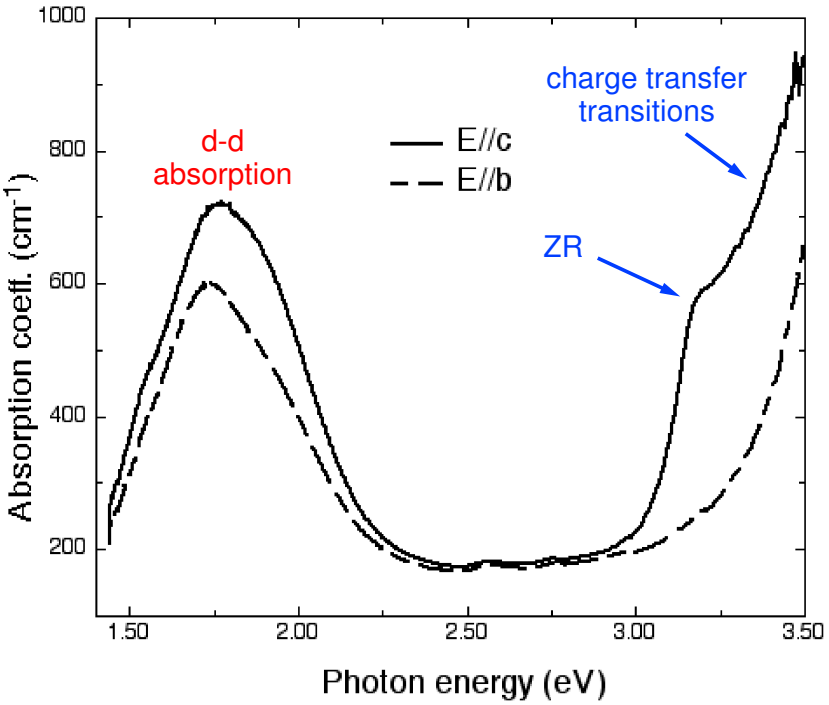


FIGURE 3.1: Absorption spectra of $CuGeO_3$ at room temperature, for both light polarization orientations [4].

## 3.1 *d-d* transitions

The feature centered at 1.7 eV in the absorption spectrum of $CuGeO_3$ (Fig. 3.1) is attributed to *d-d* transitions partially allowed by electron-phonon interactions, as demonstrated by experimental studies and ab initio calculations [3]. This spectral region has already been intensively studied and the energy positions of these structures have been calculated adopting the crystal field method [4].

The idea at the base of the crystal field theory is to view the complex system as a ionic molecule. We assume that a distribution of charges surrounding the central atom produce an electrostatic crystal field at the atom position. This is a pure electrostatic model and the central atom do not share electronic charge with its ligands. The Hamiltonian is thus composed of a free atom term $H_F$ and an additional perturbation term V(r), which accounts for the surrounding charge

distribution. The aim of this method is to evaluate the effect of the perturbation on the free atoms eigenfunctions:

$$H = \sum_i \left( \frac{p_i^2}{2m} - \frac{Ze^2}{r_i} \right) + \sum_{i<j} \frac{e^2}{r_{ij}} + \sum_i \xi\left(r_i\right) l_i s_j \tag{3.1}$$

The perturbation term is invariant under fewer coordinate transformations than $H_F$, thus reducing the site symmetry. Its effect on degenerate states is to partially or completely lift the degeneracies. In the "weak crystalline field" approximation generally adopted in the $CuGeO_3$ case, the perturbation effect is evaluated after the consideration of the Coulomb interaction effects and before accounting for the spin-orbit coupling (Eq. 3.1).

In this approximation, we initially consider not distorted $CuO_6$ octahedra in $CuGeO_3$ single crystals. In this $D_{4h}$ symmetry the $Cu^{2+}$ ion is at the center of the octahedron formed by the six O ions. The crystal field potential V(r) splits up in two terms: the first corresponding to the replacement of the six O ligands by a field with spherical symmetry, and the second accounting for the existence of the six negative charged ions at the octahedron vertices, in a cubic $O_h$ symmetry. The *d* electrons will then avoid the regions with the greatest density of ligands, thus removing their orbital degeneracy.

The Cu ion has nine *d* electrons. Based on this, the case of one *d* electron in the cubic $O_h$ field is treated but the order of the levels is rather inverted because the electrostatic field due to the ligands has an opposite effect on electrons respect to holes. The original fivefold degenerate *d* orbitals are split by the cubic field into a double degenerate $E_g$ and a threefold degenerate $T_{2g}$ orbitals. The electron densities interaction with the ligands is stronger for the $E_g$ orbitals, since directed toward the vertices of the octahedron, as shown in Fig. 3.2.

Now taking in consideration the octahedron distortion of the $CuO_6$ cluster in copper germanate, the deviation from octahedral symmetry is introduced as a change in the energies of the orbitals. The $E_g$ and $T_{2g}$ orbitals are split into four orbitals: $A_{1g}$, $B_{1g}$, which is the ground state, $B_{2g}$ and double degenerate $E_{2g}$ (Fig.

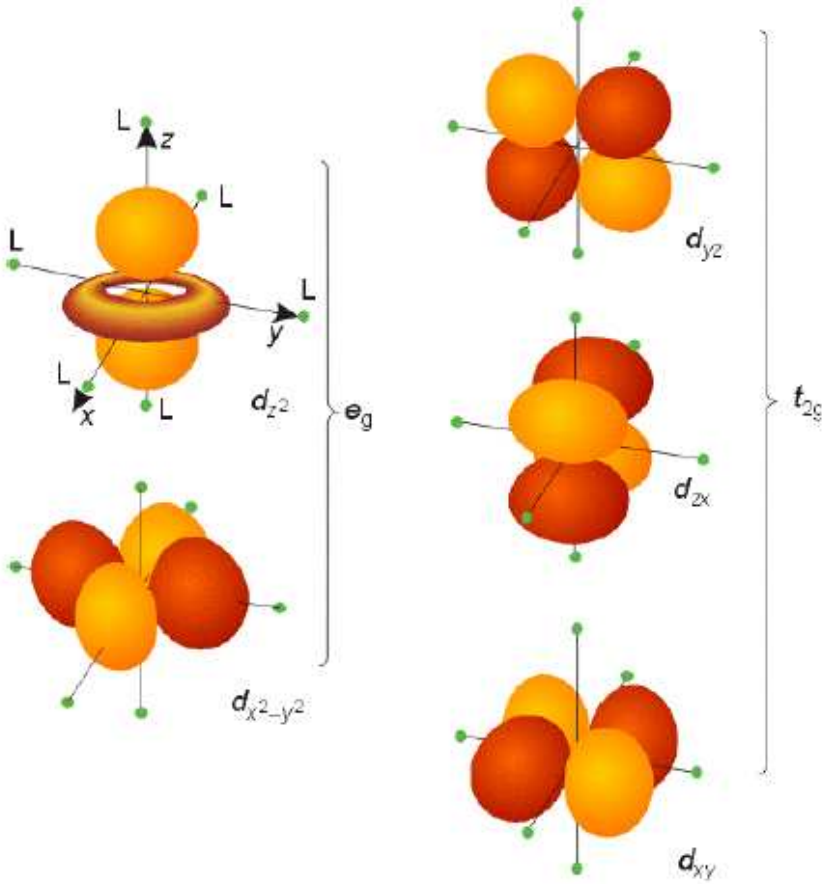


FIGURE 3.2: $E_g$ double degenerate and $T_{2g}$ threefold degenerate orbitals, originated by cubic field splitting [4].

3.3) [4, 21].

In this representation of the *d-d* energy splitting we have not considered the spin-orbit coupling. We have neglected this effect since the crystal field splitting is the dominant term in the energy level calculations for this system. The spin-orbit splitting has consequences in the calculation of X-ray absorption spectra and it removes the twofold degeneracy of the $E_{2g}$ level ($d_{yz}$ $d_{zx}$).

The attribution of this band to transitions not allowed by dipole rules is based on the observed phonon assisted character of the process [2, 20]. This is the situation expected for the *d* levels of Cu in the $CuGeO_3$ symmetry. At low temperature,

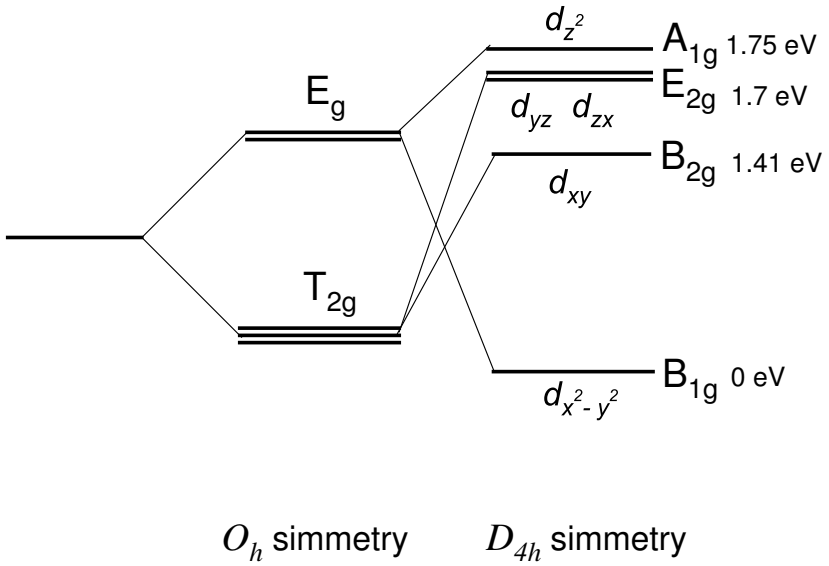


FIGURE 3.3: Crystal field splitting of a $d$ orbital in the $O_h$ and in the lowest $D_{4h}$ simmetry.

the absorption structure was found experimentally to consist of three main components, with gaussian profiles, ascribed to transitions from a ground state to three distinct levels of similar parity arising from crystal field splitting of a threefold degenerate level [4]. On the previous calculation basis, the assumption made is that the first gaussian is related to the transition from the $3d_{x^2-y^2}$ ground state to the first excited state $3d_{xy}$; the second component is the transition from the ground state to the degenerate $E_{2g}$ level and the third to the $3d_{z^2}$ state. Such a process is partially allowed when odd-symmetry perturbations are introduced in the form of electron-phonon interactions, even though forbidden by electric dipole selection rules.

The results from the crystal field method well reproduce the energy splitting between the orbitals in the $3d$ band reported from experiments and ab initio calculations [4, 3], but it does not permit us to evaluate the energy separation between the $3d^9$ and the $3^{10}\underline{L}$ excited state. On this purpose, we introduce the cluster-model calculations of the electronic structure of CuO of Eskes *et al.* [21], adapting

TABLE 3.1: Definition of the symmetry dependent charge transfer and hybridization energies [21].

| | E $3d^9$ | E $3d^{10}\underline{L}$ | $T_{pd}$ |
|---|---|---|---|
| $A_1$ | 0 | $\Delta + T_{pp}$ | $T_{pd}/\sqrt{3}$ |
| $B_1$ | 0 | $\Delta - T_{pp}$ | $T_{pd}$ |
| $B_2$ | 0 | $\Delta + T_{pp}$ | $T_{pd}/2$ |
| $E_2$ | 0 | $\Delta$ | $T_{pd}/2\sqrt{2}$ |

TABLE 3.2: Parameter values used in the $CuGeO_3$ cluster calculation [4].

| | $\Delta$ (eV) | $T_{pp}$ (eV) | $T_{pd}$ (eV) |
|---|---|---|---|
| $CuGeO_3$ | 5.2 | 0.5 | 2.5 |

the results to our $CuGeO_3$ system configuration. Eskes calculates the energy-level scheme of the one-hole basis functions before and after $Cu_{3d}$-$O_{2p}$ hybridization, on the base of a series of parameters accounting for the charge transfer energy ($\Delta$), the hybridization between the oxygen $2p$ orbitals ($T_{pp}$) and the hybridization between the $Cu_{3d}$ and the $O_{2p}$ orbitals ($T_{pd}$). The results of the one-hole problem are obtained by diagonalizing a 2x2 matrix for each energy level (simmetry):

$$\begin{bmatrix} E\,3d^9 & T_{pd} \\ T_{pd} & E\,3d^{10}\underline{L} \end{bmatrix}$$

The parameter values we use are the same adopted by Pagliara [4] in impurity cluster calculation of $CuGeO_3$ (Table 3.2).

The results from the diagonalization of the four 2x2 matrix are reported in Fig. 3.4. The energy levels for the ground state and the excited state are reported. The picture outlined gives a description of the splitting of the energy levels that does

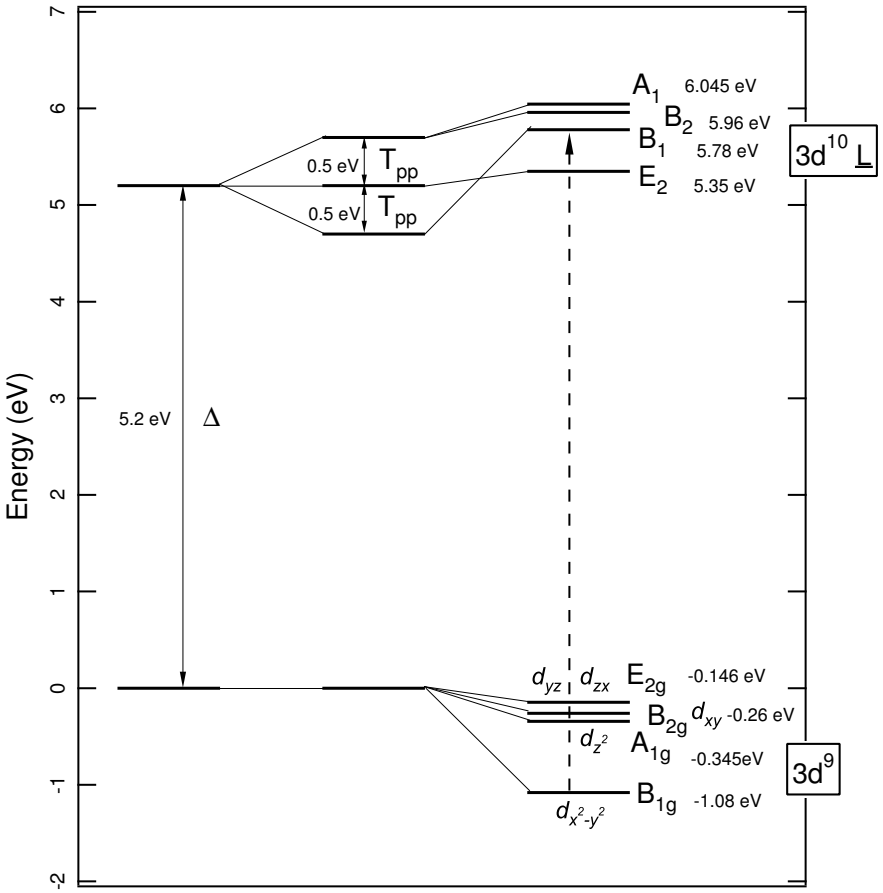


FIGURE 3.4: Energy-level scheme of the one-hole basis functions before and after $Cu_{3d}$-$O_{2p}$ hybrization. The parameters are defined in Table 3.1 and the energy levels are calculated for parameter values in Table 3.2.

not agree with the experimental results above mentioned. The energy separation is larger than the expected and the ordering of the levels is not respected. An explanation may come for the fact that in this calculations we have not considered the terms for the crystal field splitting. In the CuO case, Eskes neglects those terms because of the low energy variation they are supposed to cause. In our case the splitting for the crystal field is of the order of the energy separation found in the calculations and it can not be neglected. In this framework, the picture given by the energy level scheme does not reproduce the data found in the literature.

## 3.2 Charge transfer transitions and Zhang-Rice exciton formation

In the near-UV region of the $CuGeO_3$ spectrum in Fig. 3.1, the absorption coefficient rises exponentially with the energy. The observed absorption edge is ascribed to the onset of the charge transfer transition between the $O_{2p}$ and $Cu_{3d}$ states, as confirmed by the transition energy consistency with XPS core-line spectra [2, 20].

Pagliara et *et al.* [1, 4] first detected a structure for the $\vec{E}$ parallel to the crystal $c$ axis at 3.2 eV, just below the high absorption region. Due to the $2p - 3d$ hybridization and the strong dependence of the CT excitation on the $CuO_4$ plaquette geometry, the picture of the charge transfer alone cannot totally account for the spectrum's fine structure detail. The investigation of this optical feature showed a strong dependence on light polarization (Fig. 3.5). It has been suggested that this optical excitation is related to the chain of $Cu^{2+}$ ions running along the $c$ axis, and its weak intensity respect to the CT edge has been ascribed to the edge sharing $CuGeO_3$ structure. A temperature dependence, due to renormalization effects such as phonon-electron interactions or change in spin ordering, has also been noticed. The energy position and the strong dependence of this peak on light polarization relates this structure to the formation of a Zhang-Rice exciton [1].

Universally, exciton absorption occurs close to the fundamental absorption edge. In general, exciton are intrinsic excitations of electrons (or holes) for which a certain amount of Coulomb interaction between the pair electron-hole is retained [22, 23, 24]. The characterization of the different types of excitons is based on how far apart the electron and the hole are. Highly localized pairs correspond to the strongly bonded Frenkel type, while Wannier-Mott excitons are weakly bonded, the two particle being separated by many lattice constants. They are generally well described by a hydrogenoid model, adopting the electrons and holes effective masses. A radius $a_{exc}$ of the exciton extension in the lattice is obtained and it is

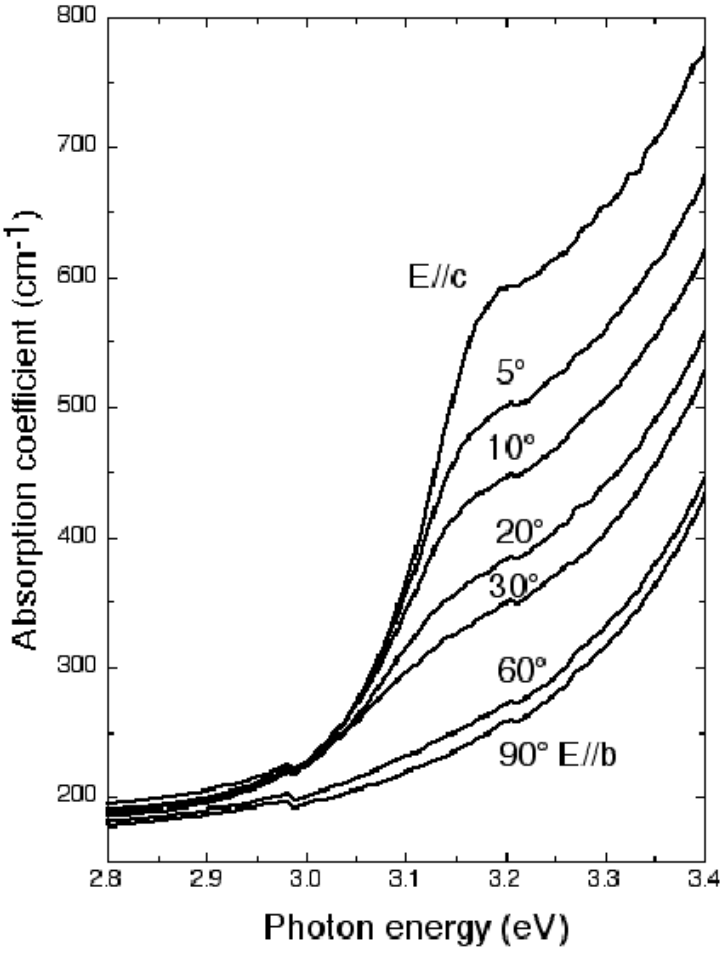


FIGURE 3.5: $CuGeO_3$ absorption spectra at room temperature for different light polarization orientation in the *b*-*c* plane. The Zhang-Rice exciton energy position is just below the CT transfer absorption edge and it strongly depends on light polarization [4].

proportional to the Bohr radius of the hydrogen atom:

$$a_{exc} = \frac{\epsilon m_0}{m_r^*} \frac{4\pi\hbar^2\epsilon_0}{m_0 e^2} \tag{3.2}$$

where $m_r^* = m_e^* m_h^* / (m_e^* + m_h^*)$ is the reduced mass and the second fraction term is the Bohr radius. The binding of the electron-hole pair strongly depends on the material's dielectric constant $\epsilon$ shielding the Coulomb interaction. For example, in classical semiconductors excitons are usually weakly bonded because of the

high dielectric constant and the small reduced effective masses. In the condition of more tightly bound band levels, the exciton becomes more localized and the Wannier-Mott picture breaks down. This is the Frenkel case of a single excited ionic level, in which the pair is sharply localized on the atomic scale. The natural scale for electromagnetic transitions between internal exciton levels is the terahertz (THz) spectral range, handling pair binding energies of few meV (1 THz $\approx$ 4 meV). Ultrafast terahertz probe have been recently employed by Kaindl *et al.* [25] to directly investigate the dynamical interplay of optically-generated excitons in semiconductors (photogenerated or introduced by doping).

The Zhang-Rice exciton does not completely fit in the above classification, being its structure composed of an electron and two neighboring holes [4]. The ZR exciton creation is based on the corresponding ZR singlet state [26, 27]. This consists of two in-plane hole orbitals: the first hole is the one created by photoexcitation on the $2p$ orbitals of the four $O^{2-}$ ions, and it is strongly bound through hybridization to the second hole, on the $Cu_{3d}$ orbital with $d_{x^2-y^2}$ symmetry ($B_{1g}$ ground state). The ZR singlet forms when an antiferromagnetic coupling is established between the Cu hole and the photoexcited O hole (see Fig. 3.6). Considering this $CuO_4$ unit cell, in the undoped case the hole is primarily localized on the Cu site, in the ground state symmetry. After the absorption of a photon, the CT electron is excited from the $O_{2p}$ to the Cu ion, and the hole is therefore at the O site. The hole introduced will reside on a linear combination of the four O sites. The Coulomb attraction between the electron and the hole is considerably large in the insulating compound, since the screening effect is weak. Due to this strong interaction and the formation of the ZR singlet, the elementary charge transfer excitation is a bound exciton of spin singlet, made up of an electron on the Cu ion and a spin singlet of Cu-O holes on the neighboring plaquette. The ZR exciton, due to its structure, can freely move through the lattice without disturbing the antiferromagnetic spin background, in contrast to the single hole motion.

In $CuGeO_3$ the low intensity of the ZR exciton absorption peak is justified by

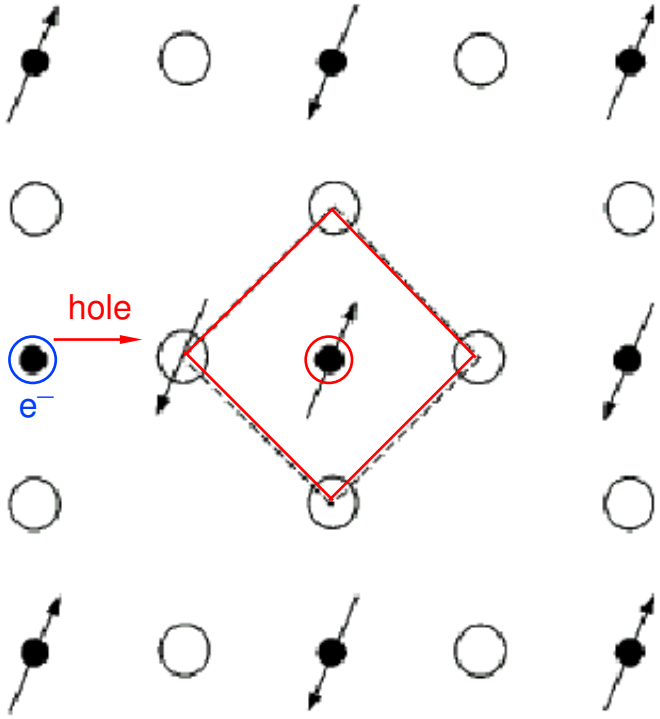


FIGURE 3.6: Zhang-Rice exciton structure in the $CuO_2$ plane. The solid circles represent the Cu ions while the open ones are the O ions. The arrows are the hole spins. The exciton is formed by the hole singlet between the Cu hole and the hole delocalized on the four ligands of the plaquette (red), and the Cu electron on the nearest neighboring $CuO_4$ plaquette (blue) [4].

the $98^0$ Cu-O-Cu angle [4]. The characteristic of the edge sharing Cu-O chains is that an O2$p$ orbital hybridizing with a $Cu_{3d}$ orbital is almost orthogonal to that of the next Cu ion. On the contrary, in the HTSC corner sharing chain a $2p$ orbital hybridizes with two neighboring $Cu_{3d}$ orbitals. This strongly influences the compound's optical conductivity. The CT excitation intensity for the edge sharing chains is smaller, due to the nature of the transition to delocalized final states. The photoinduced hole is with high probability delocalized on the nearest neighbor plaquette and the ZR exciton intensity increases with the degree of delocalization, which is maximum for a $180^0$ Cu-O-Cu angle and minimum at $90^0$.

# Chapter 4

# Transmittivity variation measurements of $CuGeO_3$

To clarify the physical mechanisms responsible for the copper germanate's optical spectral features we perform a femtosecond time-resolved spectroscopic study of the $CuGeO_3$ optical absorption, at room temperature. Focusing on the compound's absorption spectrum, we put our attention on the Zhang-Rice (ZR) exciton formation in the structure detected for the $\vec{E}$ field parallel to the $c$ crystal axis at about 3.2 eV. Our aim is to analyze the excitation and relaxation dynamics of the material in relation to the different absorption channels. On this purpose we want to photo-excite the Zhang-Rice excitons in the $CuGeO_3$ sample at a density high enough for perturbing the dielectric function of the material, and at the same time we probe the weak absorption band centered at 1.7 eV, ascribed to the copper *d-d* transitions partially allowed by electron-phonon interactions. A scheme of the energies set for the pump and probe measurement is shown in Fig. 4.1.

As further explained in the next Experimental set-up section, we pump the sample at 3.14 eV, with the second harmonic generated from the fundamental radiation of our amplified Titanium:Sapphire oscillator light source. We are next to the ZR absorption shoulder detected at 3.2 eV. The probe is performed through the

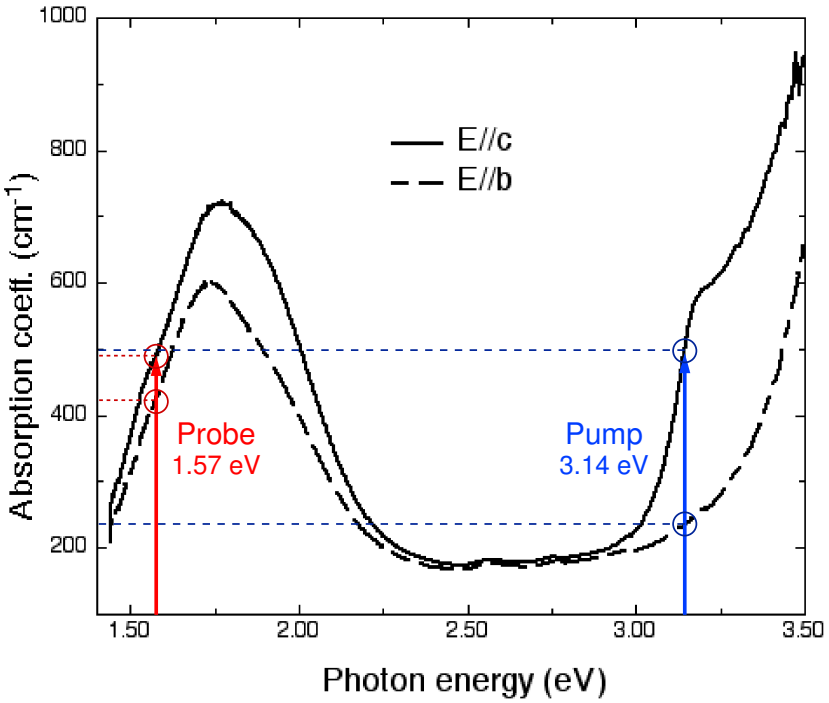


FIGURE 4.1: Scheme of the pump and probe energies adopted in the time-resolved optical spectroscopy measurements.

fundamental laser radiation at 1.57 eV, close to one end of the *d-d* absorption band. Our intention is to investigate both the configurations of pump polarization with respect to the crystal axes. From the absorption spectrum, the ZR has a strong dependence on light polarization. The absorption structure is at its maximum when the pump radiation is incident parallel to the $c$ axis of the sample, and is rapidly quenched by rotating the beam polarization axis (Fig. 3.5). With the pump beam polarized along the crystal $b$ axis, we thus expect a lower absorption, as confirmed by Pagliara *et al.* [1].

In relation to the copper germanate's optical spectrum shown in Fig. 3.1, we analyze the penetration depths of the pump and probe radiations. The penetration depth $L$ is expressed by the relation:

$$\frac{I_T}{I_0} = e^{-\alpha L} \tag{4.1}$$

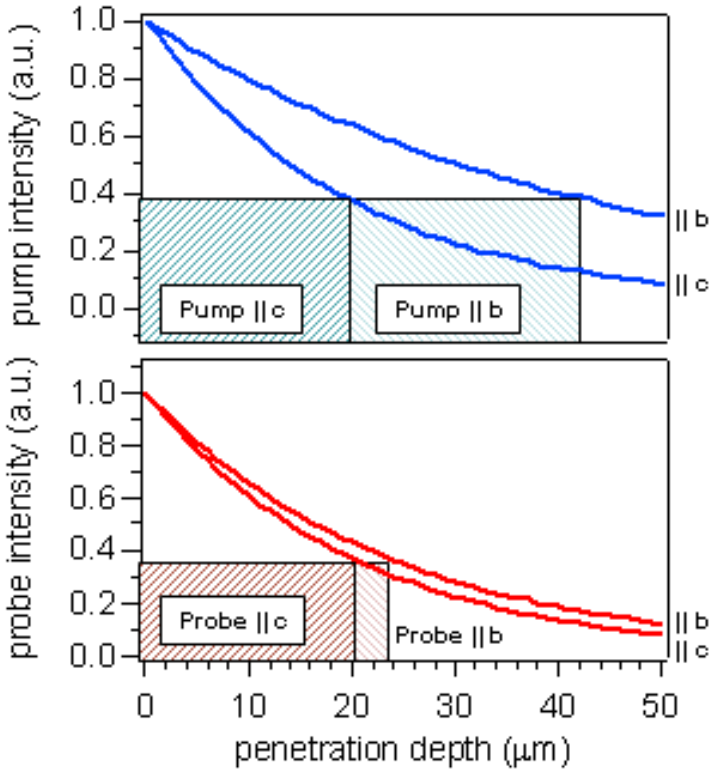


FIGURE 4.2: Comparison between the pump and the probe penetration depth in the $CuGeO_3$ sample, for the four possible configurations of polarization.

where $\alpha$ is the absorption coefficient of the material, $I_0$ is the intensity of the radiation incident on the sample and $I_T$ is the portion transmitted. Substantially, the penetration depth $L$ is the length of the material in which the exciting radiation is reduced to $1/e$ with respect to the original incident value. For the four possible configurations of polarization, the exponential decays of the intensity of the radiations penetrating in the material are compared in the scheme in Fig. 4.2. These values have to be taken into account in the evaluation of the absorption processes for $CuGeO_3$ and in the interpretation of the results from the time-resolved transmittivity variation measurements. The comparison between the region of the sample excited by the pump radiation and the region effectively probed is of great importance. In the configuration with the pump beam polarized along the crys-

tal $c$ axis, the penetration depth of the probe in both the possible orientations is comparable to the area excited at 3.14 eV. On the other hand, the quenching of the ZR structure in the pump//$b$ configuration give rise to a discrepancy, being the pumped region wider than the probed one. Since the probe transmission through the material increases when we have the pump incident on the sample in a time and spatial overlapping, this discrepancy accounts for a decrease in the probe absorption, due to the distribution of the pump energy on a wider volume of material.

The pump energy incident on the sample have to be carefully taken into consideration before performing our measurements. In order to photo-excite the Zhang-Rice excitons in the $CuGeO_3$ sample at a density high enough for perturbing the dielectric function of the material and thus have a weight in the absorption processes, we need about 300 mJ/(cm$^2\cdot$ pulse) of incident pump fluence at 3.14 eV. In the pump//$c$ configuration, this value corresponds to a photo-doping percentage $n_{\%}$ of the material of about 3.5%. The calculation follows from the ratio between the number of photons/(cm$^3\cdot$ pulse) and the $CuGeO_3$ density $n_{CuGeO_3}$ ($8.4\cdot10^{21}$ cm$^{-3}$):

$$n_{\%} = 0.3\left[\frac{J}{cm^2\cdot pulse}\right]\cdot\frac{1}{1.6\cdot10^{-19}\left[\frac{J}{eV}\right]\cdot 3.14\,[eV]}\cdot\alpha\cdot\frac{1}{n_{CuGeO_3}} =$$

$$= 5.97\cdot10^{17}\left[\frac{photons}{cm^2\cdot pulse}\right]\cdot 500\left[cm^{-1}\right]\cdot\frac{1}{8.4\cdot10^{21}\,[cm^{-3}]}\approx 3.5\% \qquad (4.2)$$

We evaluate the 500 cm$^{-1}$ pump absorption $\alpha$ from the recent studies carried on $CuGeO_3$ by Pagliara *et al.* [4]. The crystal sample we use in the measurements results to be fragile for fluences above the 300mJ/(cm$^2\cdot$pulse) value. All these measurements should also be performed exciting the sample for the shortest interval possible, since its fragility comes up as soon as we employ a slightly higher pump fluence or after focusing the radiation (see Sec. 5) on the same spot for too long. The spot under investigation may quickly break down, showing a noticeable continuous loss of transmitted signal.

Our investigation of the $CuGeO_3$ optical properties begins with the study of the linearity of the transmitted signal through the sample versus the reference incident intensity for both the pump and the probe radiations, in the above mentioned configurations of polarization. Our intention is to analyze whether a non-linearity in the absorption, with a two-photons process, is present and how influences the subsequent time-resolved measurements. In the whole investigation, either for non-linearity absorption studies or for time-resolved spectroscopy, we only measure the transmitted signal, disregarding the portion of radiation reflected by the sample. The reflected signal does not influences the absorption evaluation since its variation in function of the incident power results to be negligible.

Through a pump and probe technique we then perform the time-resolved transmittivity variation measurements. We carry out a series of measurements varying the pump incident power. Our analysis is focused on the four possible configurations, following the linear polarization orientations of the pump and probe beams with respect to the crystal axes. This is done to clarify how the ZR formation and the phonon-assisted *d-d* transitions enter in the excitation and relaxation dynamics. An evaluation of the relaxation life-times of the system is needed to understand what processes follow the photo-doping with the ZR excitons creation.

# Chapter 5

# Experimental set-up

In this section we report the description of the experimental set-up developed for time-resolved optical spectroscopy measurements, as shown in Fig. 5.1.

The light source is an amplified Ti:Sapphire laser system, with a central wavelength of 790 nm, a pulse time-width of 160 fs, 1 kHz repetition rate and an output power of 300 mW. As illustrated in Sec. 4, the pump-probe experiment is performed with a probe photon energy h$\nu$=1.57 eV corresponding to the laser fundamental radiation, and a pump photon energy h$\nu$=3.14 eV, obtained by duplicating the frequency of the fundamental with a BBO crystal.

The first stage is a Mach-Zehnder interferometer: a small portion of the laser radiation is reflected by a UVFS wedge beam splitter (BS) and is used as the probe; a delay time $\tau$ is introduced between the *pump* and *probe* pulses through a delay stage, constituted by two metallic mirror mounted on a linear translator with a minimum step of 40 nm (0.13 fs). The probe beam is then directed to the $CuGeO_3$ sample through a half-wave plate and a polarizer (Pl+$\lambda$/2 @800nm), to control both beam intensity and polarization.

On the other optical branch, before the second harmonic generation process (SHG), the pump passes through a telescope made up of two lenses with focal lengths $f_1$=300 mm and $f_2$=-75 mm, respectively. The main reason for introducing

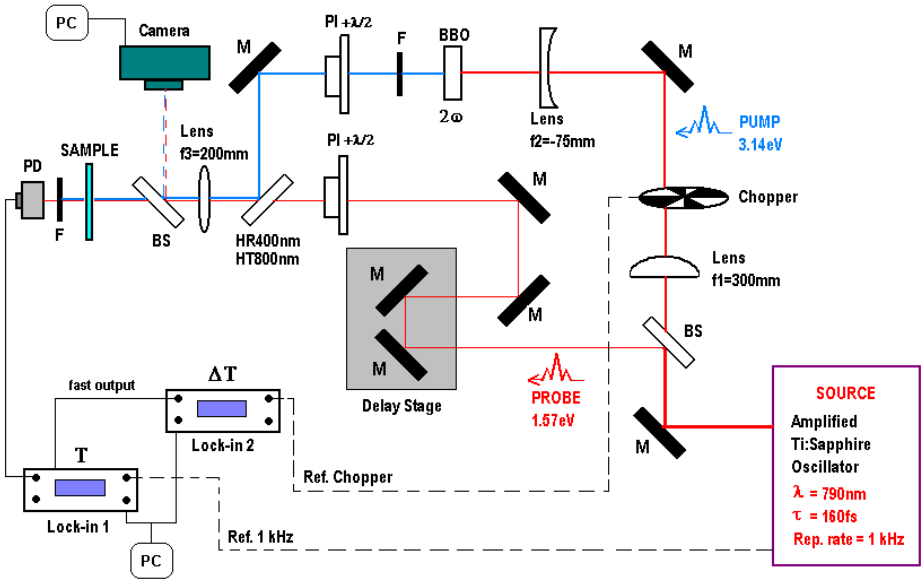


FIGURE 5.1: Experimental set-up for time-resolved optical spectroscopy. The set-up is configured for time-resolved transmittivity variation measurements, with two lock-ins signal acquisition system.

this optical element is directly related to the pump energy needed to perform the time-resolved measurements, as introduced in Sec. 4.

In order to photo-excite the Zhang-Rice excitons (ZR) in the $CuGeO_3$ sample at a density high enough for perturbing the dielectric function of the material, we need about 300 mJ/cm$^2$ of pump output fluence at 3.14 eV from the SHG process. With a focused spot size of 60x60 $\mu$m$^2$, this corresponds to a pump output power of 10 mW. On this purpose, it is important to concentrate on two aspects: the size of the fundamental beam incident on the non-linear crystal and the conversion efficiency $\phi$ of the SHG process. Both these aspects have to be carefully taken into account in the development of the experimental set-up, in order to produce 300 mJ/cm$^2$ of pump energy from the SHG process without damaging the non-linear crystal. For the SHG we employ a type I BBO crystal, 0.3 mm thick and cut at an angle of $30^0$. The phase-matching angle $\theta$ for the radiation at 800 nm is $29.6^0$. The damage threshold for the non-linear crystal is about 100 GW/(cm$^2$·pulse). The

peak intensity $I_{peak}$ of the fundamental radiation is given by:

$$I_{peak}\left[\frac{W}{cm^2 \cdot pulse}\right] = \frac{P_\omega}{Rep.Rate \cdot \tau_{pulse} \cdot A_{spot}} \tag{5.1}$$

where $P_\omega$ is the incident power of the fundamental radiation, *Rep.Rate* is the laser system repetition rate, $\tau_{pulse}$ is the pulse time-width and $A_{spot}$ is the beam spot size.

Following Eq. 5.1, we make use of the telescope described above to reduce the fundamental beam spot size, thus optimizing the $I_{peak}$. The telescope reduces the 6.5 mm fundamental spot diameter to 1/4 of its original size. By considering an incident power $I_\omega$ of about 100 mW we obtain an incident pulse peak intensity $I_{peak}$ of about 30 GW/cm$^2$, which is below the crystal damage threshold. In this configuration we measure a process conversion efficiency $\phi$ of about 10%. Introducing the expression for the calculation of $\phi$, we obtain:

$$\phi = \frac{I_{2\omega}}{I_\omega} = \frac{n_{2\omega}}{2Z_0}\frac{\left|\vec{E}_{2\omega}\right|^2}{I_\omega}$$

$$= \frac{2Z_0}{n_\omega^2 \cdot n_{2\omega}}\, I_\omega \left(2\pi \cdot \chi^{(2)} \cdot \frac{L}{\lambda}\right)^2 \cdot \mathrm{sinc}^2\left(\frac{\Delta K \cdot L}{2}\right) \tag{5.2}$$

$$= \frac{2 \cdot 377}{(1.5)^3}\, 33 \cdot 10^{13}\left[\frac{\mathrm{W}}{\mathrm{m}^2}\right]\left(2\pi \cdot 1\left[\frac{\mathrm{pm}}{\mathrm{V}}\right] \cdot \frac{0.3\mathrm{mm}}{790\mathrm{nm}}\right)^2 = 42\%$$

where $Z_0$ is the vacuum impedance $\sqrt{\mu_0/\epsilon_0}$, $L$ is the crystal length and $\Delta K = 0$ is the phase-matching condition. The low conversion efficiency we obtain in the SHG process, with respect to the calculated one, is ascribed to the fact that the laser beam is not focused on the BBO crystal, but it is only reduced in size by the telescope, and that in the $\phi$ expression we neglect the terms accounting for gaussian beams. In this framework, the 10% conversion efficiency is justified. Moreover, this $\phi$ value enables us to obtain the desired pump output power without damaging the BBO crystal.

Another purpose for adopting the telescope with these focal lengths is to have the size of the pump gaussian beam larger than the probe when both focused on

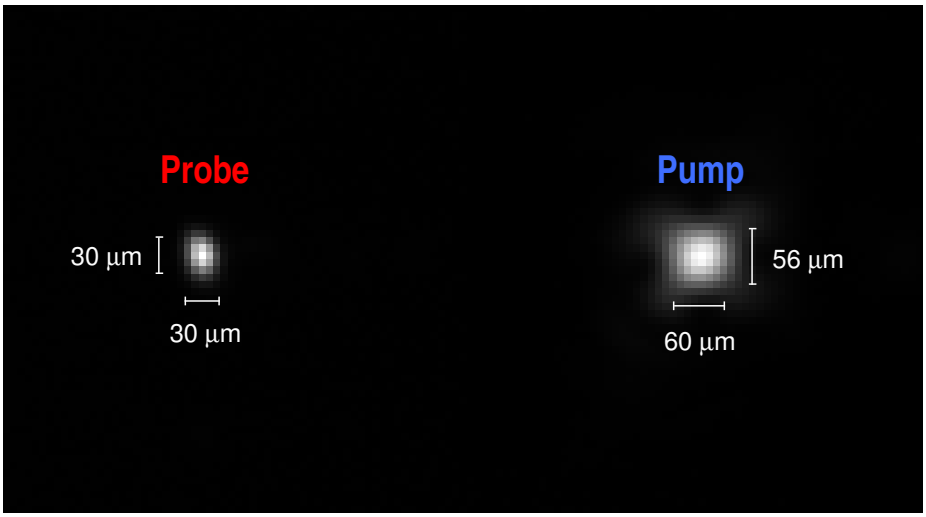


FIGURE 5.2: Gaussian profiles of the pump and probe spots incident on the $CuGeO_3$ sample.

the sample by the same lens, in order to probe a spatially uniform excited region. As stated by the following equation, the beam size in the focal plane is:

$$d_{focus} = \frac{4\lambda f}{\pi d} \tag{5.3}$$

where $d_{focus}$ is the spot diameter at the focal plane, $\lambda$ is the radiation wavelength, $f$ is the lens focal length and $d$ is the incident beam diameter. By considering a 400 nm pump beam, with an incident diameter of 1.625 mm, we obtain a pump spot size at the focal plane of 56x60 $\mu m^2$; while the 800 nm probe is 30x30 $\mu m^2$ large, in agreement with Eq. 5.3. Their gaussian profiles are shown in Fig. 5.2.

This configuration assures that the spatial region probed in the transmittivity measurement has been uniformly excited by the pump pulse, avoiding any problems due to slight misalignment of the two beams during the experiment. A CCD camera is used to monitor the beam profiles, the mutual positions and the spot sizes of the two pulses.

The pump radiation is then duplicated in frequency with the BBO crystal, it's filtered (F) to eliminate the fundamental wavelength in the output light and it goes through a polarizer-half-wave plate system (Pl+$\lambda/2$ @400nm), to control

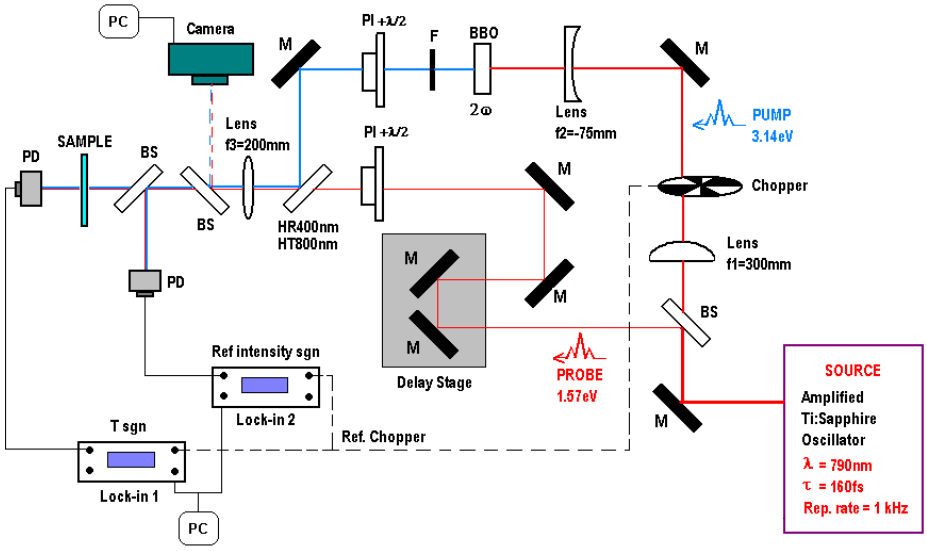


FIGURE 5.3: Experimental set-up configured for non-linear absorption measurements to verify the behavior of the pump and probe sample transmittivity versus the reference intensity, with one lock-in signal acquisition system.

both intensity and polarization. Finally the two pulses recombine on a HR400nm-HT800nm plate and, in a collinear configuration, they are both focused on the sample by the same lens with focal length $f_3$=200 mm, mounted on a 3-degrees of freedom translation stage. The sample itself is located on a rotation stage, useful to match the crystal axes with the beams polarization axes, and it is brought in the lens focal plane by a linear translator.

In the configuration for non-linear absorption measurements (Fig. 5.3), the pump beam and the probe beam are alternatively stopped to verify the behavior of the transmittivity versus the incident light intensity, at the wavelength of the radiation exciting the $CuGeO_3$ sample. The beams are chopped at about 250 Hz before exciting the sample. The radiation intensity is varied acting on the Pl+$\lambda/2$ systems. The intensity of the transmission of the beam through the sample, together with the reference signal intensity, are acquired on a PC by means of a photodiode and a lock-in amplifier referenced to the trigger of the chopper.

We adopt a lock-in amplifier to make use of its frequency selection technology

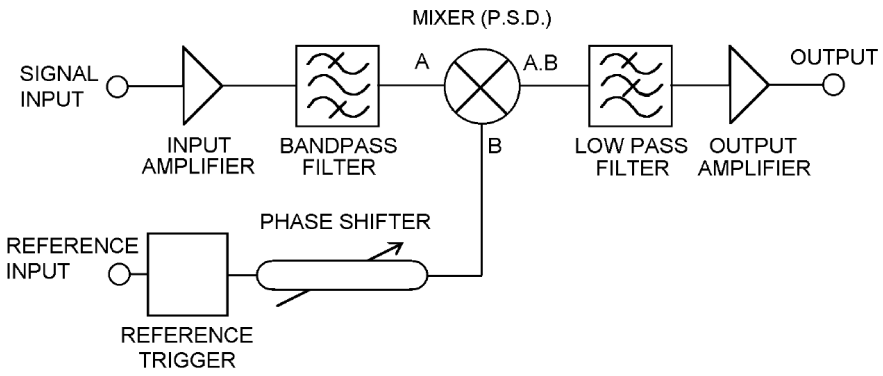


FIGURE 5.4: Lock-in amplifier diagram [28].

in the optimization of the signal-to-noise ratio when acquiring the radiation signal collected by the photodiode (Fig. 5.4). Its properties are based on a phase-sensitive detector (PSD) that converts the input alternate current signal (AC) into a proportional DC signal, with the advantage of straightening only the signal spectral component close to the reference frequency $\omega$ we provide to the instrument. All the spectral noise not centered at $\omega$ remains AC modulated and it is removed by a low-pass filter. The PSD multiplies two signals: the one acquired in the input channel (experimental signal) and the sinusoid generated from the reference trigger with frequency equal to the reference signal. The sinusoid created is phase locked to the input signal itself. In this way the PSD reveals every variation in the frequency of the measured signal, being the reference phase-locked to it [28]. In the above mentioned configuration, the input and the reference signal have the same frequency but a relative phase that varies, following the phase shift $\theta$ introduced by the experiment. In the reference channel, a phase shifter compensates for $\theta$. Writing the expression for the input signal and for the reference:

$$V_{in} = A\cos(\omega t + \theta) \tag{5.4}$$

$$V_{ref} = B\cos(\omega t) \tag{5.5}$$

The PSD operates multiplying the two signals:

$$V_{PSD} = A\cos(\omega t + \theta) \cdot B\cos(\omega t) \tag{5.6}$$

$$= AB\left(\cos^2(\omega t)\cos\theta - \cos(\omega t)\sin(\omega t)\sin\theta\right)$$

$$= AB\left[\left(\frac{1}{2} + \frac{1}{2}\cos(2\omega t)\right)\cos\theta - \frac{1}{2}\sin(2\omega t)\sin\theta\right]$$

$$= \frac{1}{2}AB\cos\theta + \frac{1}{2}AB\cos(2\omega t + \theta)$$

The amplitude $B$ of the reference sinusoid is held constant. The result is a signal proportional to the input amplitude $A$ and to $\theta$, with a frequency doubled with respect to the acquired signal. A low-pass filter removes the $2\omega t$ component and the surrounding spectral noise, returning the noise-free DC component as the output of the lock-in amplifier.

In the configuration for time-resolved transmittivity variation measurements (Fig. 5.1), the pump and probe pulses are time and spatially overlapped on the $CuGeO_3$ sample. We check the overlapping by means of a sum-frequency generation process (SFG). On this purpose, we replace the $CuGeO_3$ sample with a type I BBO crystal, 0.3 mm thick, cut at an angle of $46^0$. The phase-matching angle $\theta$ for the radiation wavelengths considered is $45.1^0$. The optimal time and spatial overlap of the 395 nm-pump and 790 nm-probe pulses is obtained optimizing the intensity of the 263 nm sum-frequency radiation generated in the non-linear process. As shown in Fig. 5.5, we focus the pump and probe beam on the BBO crystal and disperse the transmitted radiation through a prism (Pr). Then a $f_3$=200 mm lens focuses the beam on a photodiode. A pin-hole (Ph) is used to filter the SF generated radiation and the signal is recovered by a lock-in amplifier connected to a PC and referenced to the laser system 1 kHz-trigger. The optimization of the SFG signal is obtained acting on the HR400nm-HT800nm plate.

Another important feature of this procedure is that we can measure and monitor the time-width of the pulse exciting the sample. By controlling the delay stage

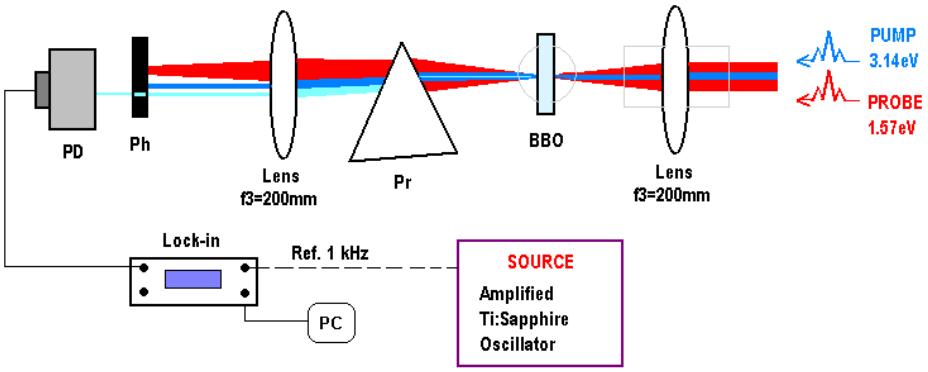


FIGURE 5.5: Set-up section for the sum-frequency generation process, adopted to check the pulses time and spatial overlapping and to measure the time-width of the pulse exciting the sample.

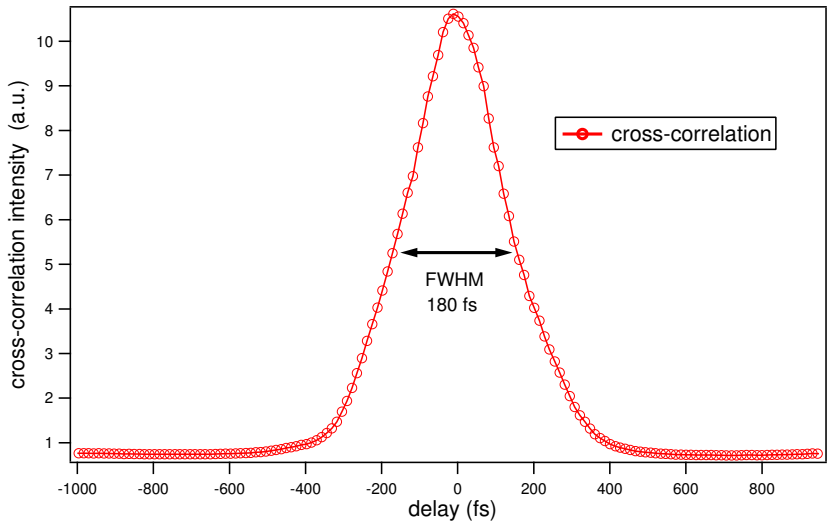


FIGURE 5.6: Cross-correlation profile of the pulse exciting the sample. We measure a pulse time-width of 180 fs.

mounted on the probe optical branch, a background-free intensity cross-correlation of the SFG signal is obtained. A profile of the cross-correlation is shown in Fig. 5.6: the FWHM pulse time-width is about 180 fs.

For time-resolved transmittivity variation measurements we place the $CuGeO_3$ sample in its original position. The mechanical chopper is set on the 3.14 eV-pump beam at a frequency of about 40 Hz. The intensity of the transmission of the probe

through the sample is now recovered with a photodiode and a system of two lock-in amplifiers. By using as a reference the 1 kHz-trigger of the Ti:S laser system, the first lock-in amplifier operates a fast integration of the transmittivity signal ($T$) at the probe wavelength, with a 640 $\mu$s time constant. The output is acquired on the second lock-in, referenced to the 40 Hz-trigger of the chopper, which directly measures the variation of transmittivity ($\Delta T$) at the probe wavelength, induced by the pump exciting the sample. The second lock-in time constant is set to 200 ms, performing a slow integration in order to reduce the signal to noise ratio. Both $\Delta T$ and $T$ are acquired on a PC. Finally, we divide the two signals to obtain the relative transmittivity variation ($\Delta T/T$).

The sample used for the experiments is a high-quality $CuGeO_3$ single crystal, few millimeters long, translucent and of a light blue color. It is grown from the melt by a floating zone technique and it is cleaved perpendicular to the $a$ axis, along the $b$-$c$ plane [29].

# Chapter 6

# Results and Discussion

Optical absorption properties of $CuGeO_3$ are investigated through time-resolved optical spectroscopy measurements. We study two aspects of the material's optical properties:

- As preliminary measurements, we investigate the linearity of the optical absorption. We study the pump (3.14 eV) beam absorption and the probe (1.57 eV) beam absorption as a function of the incident intensity, up to the damage treshhold.

- We perform time-resolved transmittivity variation measurements. Through a pump and probe technique, we study the effects of the photo-excitation of the Zhang-Rice excitons in the sample on the absorption dynamics in the $d$-$d$ transitions energy region at 1.57 eV. The measurements are carried out in the four possible linear polarization orientations of the pump and the probe beams with respect to the crystal axes. For each of these configurations, we perform a series of measurements varying the pump incident power. The overall discussion and interpretation of the excitation and relaxation dynamics are reported.

## 6.1 Non-linear absorption measurements

The experimental set-up for non-linear absorption measurements has been described in the previous section. By varying the laser fluence, we study the linearity of the absorption process of $CuGeO_3$ when excited at different radiation frequencies. In order to check the linearity of the experimental system, we perform a calibration after having removed the $CuGeO_3$ sample. Varying the probe radiation (1.57 eV) intensity through the Pl+$\lambda/2$ system (Fig. 5.3), we recover the signal incident on the photodiode versus the reference intensity. The reference signal has been calibrated with a power meter, in order to plot the detected signal as a function of the incident intensity in mJ/cm$^2$. To increase the signal-to-noise ratio we average a plateau of points for each radiation intensity level.

We repeat the same measurement for the pump beam (3.14 eV). As shown in Fig. 6.1, the linearity of the experimental system is confirmed. By fitting the data with a quadratic function:

$$y = a + bx + cx^2 \tag{6.1}$$

where $a$, $b$ and $c$ are free parameters of the fit, we obtain that the second order coefficient $c$ is approximately null and the trend is linear.

After the verification of the linearity of the set-up, we investigate the linearity of the $CuGeO_3$ absorption of the probe radiation, in the energy range we operate ($h\nu$=1.57 eV, $h\nu$=3.14 eV) in the subsequent time-resolved measurements. Acting on the Pl+$\lambda/2$ system we are able to align the beam polarization axis parallel to one of the crystal axes of the sample. By measuring the sample absorption parallel to the $c$ axis, we investigate the configuration of maximum optical absorption, as illustrated in Sec. 3. Then rotating the beam polarization axis by $90^0$ we probe the $b$ axis of minimum absorption. To optimize the alignment we look at the value of the transmitted radiation intensity, maximizing or minimizing it by slightly rotating the sample in the $b$-$c$ plane through the rotation stage.

The results for the probe in the two configurations of polarization are shown in

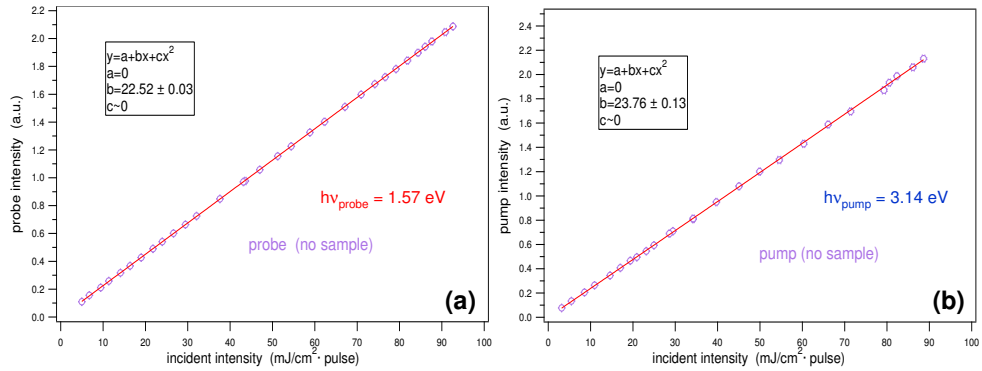


FIGURE 6.1: Experimental set-up calibration. The $CuGeO_3$ sample has been removed and both the probe (a) and the pump (b) intensities versus the reference signal have been measured. The quadratic fitting equation (red line) and the coefficients are reported.

Fig. 6.2. In the probe intensity range used in the experiment the absorption is linear and no other relevant features are evidenced. This result indicates that, during the time-resolved measurements, no contribution from multiphoton absorption of the probe pulse has to be considered. On the contrary, a non-linear behavior in both polarization orientations is evidenced when we repeat the same measurements for the absorption of the pump radiation. In Fig. 6.3 the pump intensity transmitted through the sample is plotted versus the incident beam reference intensity. The evident non-linear behavior is the signature of a multiphoton absorption process. In particular, the experimental data can be fitted with a quadratic function, indicating a 2nd-order absorption process at $2h\nu$=6.28 eV. The value of the coefficients are reported in Fig. 6.3. We can estimate the energy involved in the non-linear process by considering the deviation of the fit from a linear function tangent to the origin (dashed line in Fig. 6.3). In particular, at a pump fluence of 70 mJ/cm$^2$, the 2nd-order energy absorption $\Delta_2$ is approximately 10% of the total energy.

In the next paragraph we will discuss the influence of the non-linear absorption process on the time-resolved measurements.

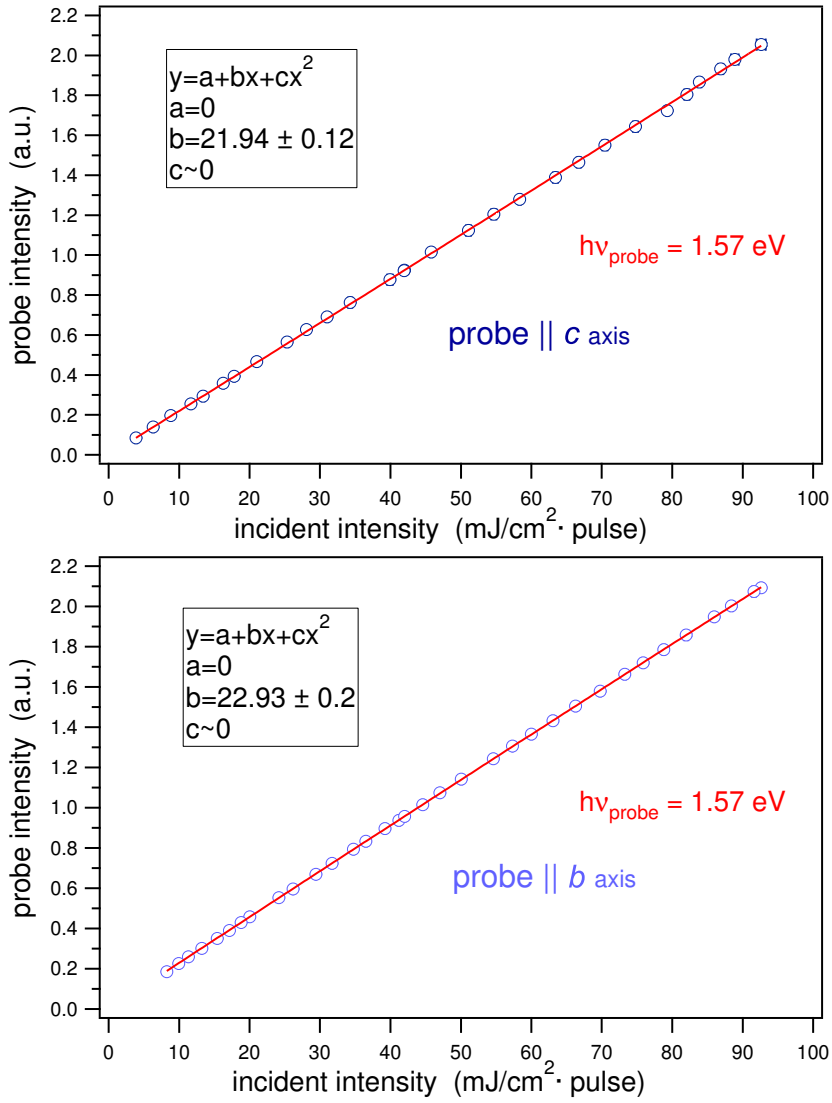


FIGURE 6.2: $CuGeO_3$ absorption measurements of the probe radiation. The probe transmitted intensity versus the incident intensity have been investigated, in both polarization orientations with respect to the crystal axes. (a) probe polarized parallel to the crystal $c$ axis. (b) probe polarized parallel to the crystal $b$ axis. The quadratic fitting equation (red line) and the coefficients are reported. The probe absorption is linear.

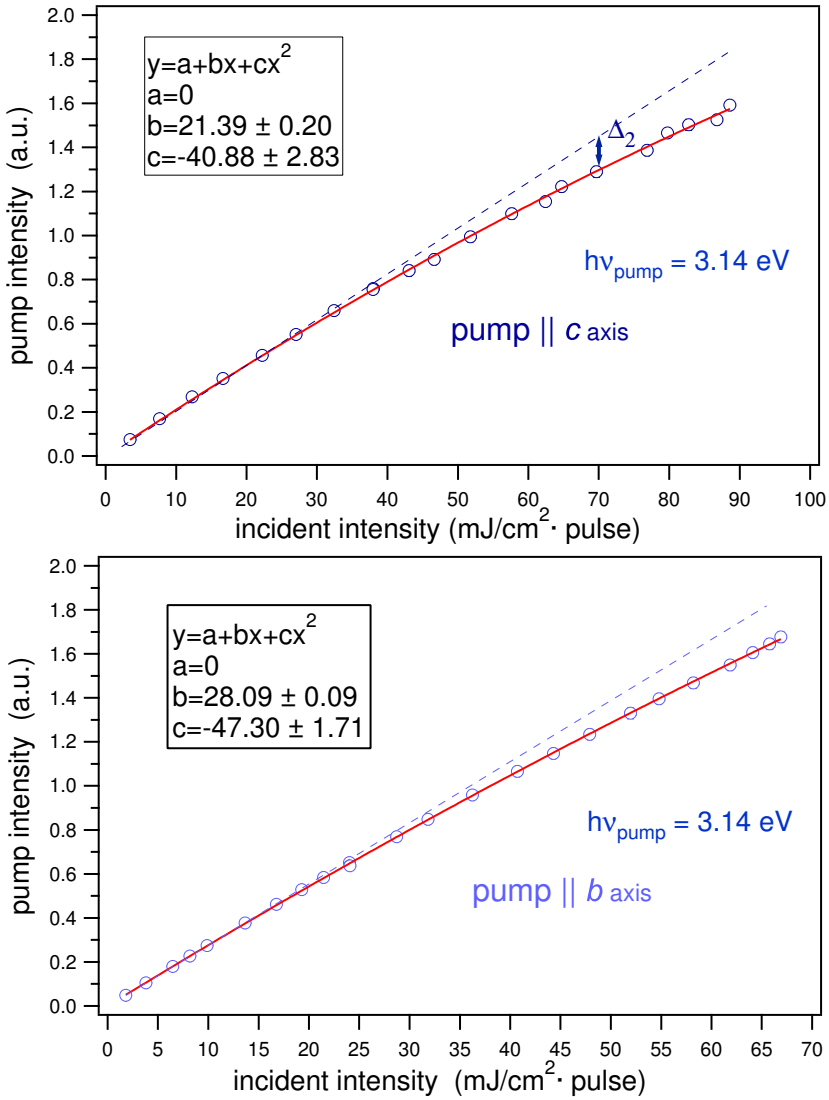


FIGURE 6.3: $CuGeO_3$ absorption measurements of the pump radiation. The pump transmitted intensity versus the incident intensity have been investigated, in both polarization orientations with respect to the crystal axes. (a) pump polarized parallel to the crystal $c$ axis. (b) pump polarized parallel to the crystal $b$ axis. The quadratic fitting equation (red line) and the coefficients are reported. The second order coefficient is non-vanishing, thus the pump absorption is non-linear.

## 6.2 Time-resolved optical measurements

Through a pump and probe technique, we now perform the time-resolved transmittivity variation measurements.

### 6.2.1 Time-resolved transmittivity variation

In order to study the effects of the high-density photo-excitation of the Zhang-Rice excitons on the electronic properties of the $CuGeO_3$ sample, we pump the material at 3.14 eV and we analyze the response of the sample at 1.57 eV, in the energy region ascribed to the phonon assisted *d-d* transitions (see Sec. 4).

The intensity of the pump radiation is about 180 mJ/cm$^2$ and is reported on both graphs in Fig. 6.4. The percentage of the photodoping $n_{\%}$ induced by pump excitation at this intensity is about 2% and can be calculated from the ratio between the number of photons/(cm$^3$·pulse) absorbed by the $CuGeO_3$ crystal and the density of the material ($8.4{\cdot}10^{21}$ cm$^{-3}$), as explained in detail in chapter 4.

$$n_{\%} = E_{in}\left[\frac{J}{cm^2 \cdot pulse}\right] \cdot \frac{500\left[cm^{-1}\right]}{1.6 \cdot 10^{-19}\left[\frac{J}{eV}\right] \cdot 3.14\,[eV]} \cdot \frac{1}{8.4 \cdot 10^{21}\,[cm^{-3}]} \qquad (6.2)$$

The results of the measurements are presented in Fig. 6.4a. The pump and probe electric fields are polarized parallel to the crystal *c* axis, in order to maximize the formation of the Zhang-Rice excitons. The percentage variation of probe transmittivity ($\Delta T/T$) is plotted versus the time delay between the pump and probe pulses. The $\Delta T/T$ values are negative, thus the sample absorption increases when the interaction with the pump radiation takes place.

We observe two different dynamics in the absorption process: a small background is followed by an absorption peak with a gaussian-like profile and a time duration slightly longer than the 180 fs cross-correlation profile (light blue line). In this configuration of maximum absorption, the transmittivity variation reaches

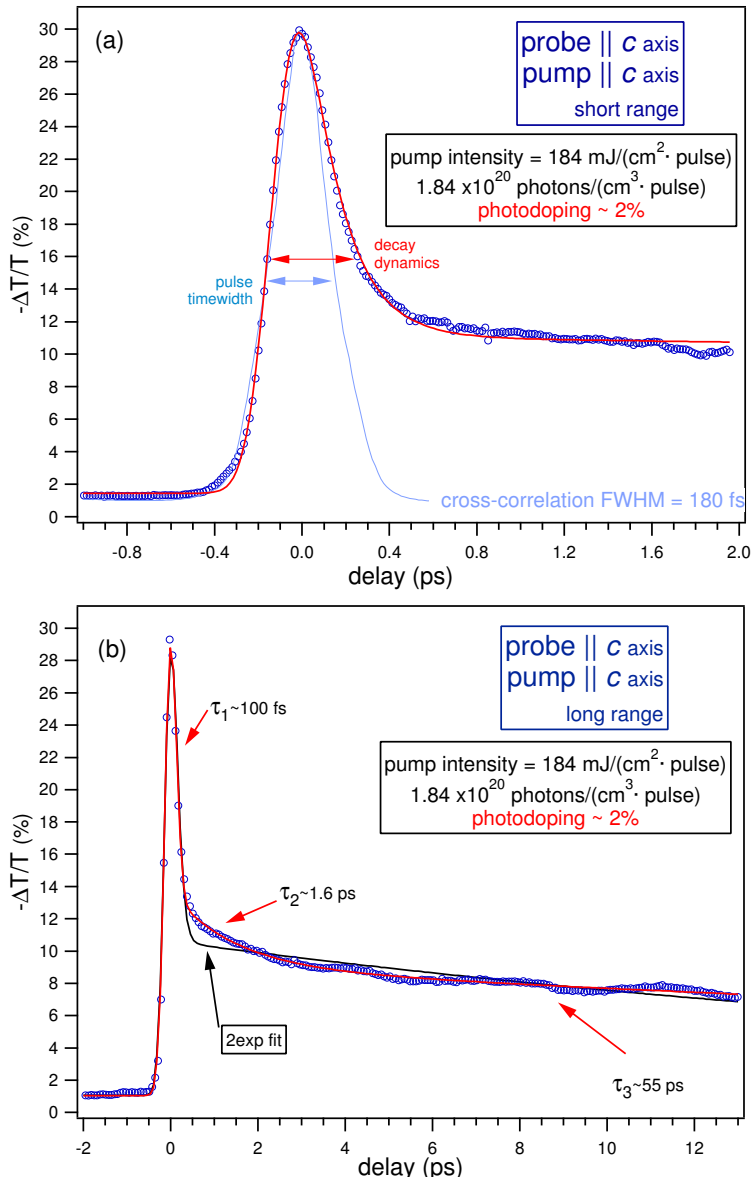


FIGURE 6.4: Time-resolved transmittivity variation measurement. The pump and probe are polarized along the $c$ axis. (a) Short range measurement. The $\Delta T/T$ percentage variation is plotted versus the delay of the time-resolved measurement. The data are fitted by a gaussian convoluted with a double exponential (red line). The fast interaction peak (blue marks) is compared with the gaussian cross-correlation profile (light blue line). (b) Long range measurement. The data are fitted by a gaussian convoluted with a triple exponential (red line). The fit to data with a gaussian convoluted with a double exponential (black line) is also shown for comparison.

values as high as the 30%. In the picosecond time-scale the signal slowly decays up to a 11% value. We note that the detected transmittivity variation is much larger than the estimated photodoping percentage, suggesting that a deep modification of the properties of the system is induced by the pump excitation.

In order to extract information on the measured dynamics we fit data with a function $f(t)$ composed by a gaussian $G(t)$, accounting for the pulse time-width of 180 fs, convoluted with two exponentials $Exp(t)$, which describe the relaxation of the system. The expression is given by:

$$G(t) = \frac{1}{\sigma\sqrt{2\pi}}\, e^{-\frac{(t-t_0)^2}{2\sigma^2}}$$

$$Exp(t) = A_1 e^{-\frac{t-t_0}{\tau_1}} + A_2 e^{-\frac{t-t_0}{\tau_2}} \tag{6.3}$$

$$f(t) = \int_{\Delta t} \left(G(t') \cdot Exp(t-t')\right)\, dt'$$

where $\sigma$ is the gaussian time duration and $\tau_1$, $\tau_2$ are the exponential time-constants. The integral is performed over the time interval of the measurement. From the fit we obtain $\tau_1 \simeq$100 fs and $\tau_2 \simeq$1.6 ps. The measured background is the signature of a non complete relaxation of the system before the arrival of the next excitation pulse ($\Delta t$=1 ms @ 1 kHz repetition rate). The positive-delay dynamics is related to a modification of the physical properties of the system as a consequence of the excitation at $h\nu$=3.14 eV. In particular the fast dynamics, which is of the order of the pulse time-width, is faster than any possible interaction between the excited electron system and phonons. In other words, 100 fs is a time too short to induce a modification of the structural properties of the system, unless they originate from electronic response (e.g. see GaAs). As a consequence it is likely that the fast relaxation can be related to a direct modification of the electronic band structure as a consequence of the pump excitation.

In order to deeply investigate the slow relaxation dynamics, the transmittivity variation is measured on a longer time scale (∼15 ps), as reported in Fig. 6.4b. The pump intensity and, as a consequence, the photo-doping percentage is the

same as the previous measurement.

In this case, a double exponential decay is not a satisfying approximation of experimental data, as evident from Fig. 6.4b (the double-decay fit is the black solid line). As a consequence the data has been fitted by a gaussian convoluted with three exponential functions. The third exponential decay is added in the $Exp(t)$ function and a further $\tau_3$ exponential life-time is introduced. In order to obtain a reliable value for the three time-constant, we keep fixed the $\tau_1$ value obtained from the fit to the short range measurement, while we leave as free parameters the $\tau_2$ and $\tau_3$ values. According to the previous result, the life-time $\tau_2$ of the slow relaxation tail feature is evaluated in about 1.5 ps. A longer time range relaxation follows right after and it is individuated by a $\tau_3$ life-time of the order of 50 ps. It is important to note that, in order to obtain a reliable value for the time-constant $\tau$ of an exponential decay, a time-window greater than $3\tau$ is needed. In our case, on the contrary, the time-window of the measurement is smaller than $\tau_3$. As a consequence, the $\tau_3$ value is only indicative of a relaxation of the system much slower than the time-scale accessible to the present measurements. In any case this slow decay can be interpreted as the relaxation of the system to the equilibrium conditions before the pump excitation.

### 6.2.2 Polarization dependence of relaxation dynamics

The role played in the transmittivity variation by the Zhang-Rice excitons formation, can be investigated by analyzing the polarization dependence. In fact, as explained in chapter 3, the excitation of the Zhang-Rice singlet is strongly dependent on light polarization, whereas the direct charge-transfer process between the $O_{2p}$ and $Cu_{3d}$ levels is not subjected to selection rules.

For this reason we performed time-resolved transmittivity measurements in four possible configurations, changing the linear polarization orientations of the pump and probe beams with respect to the crystal axes of the sample. The pump and probe incident power on the sample are held constant. The results are pre-

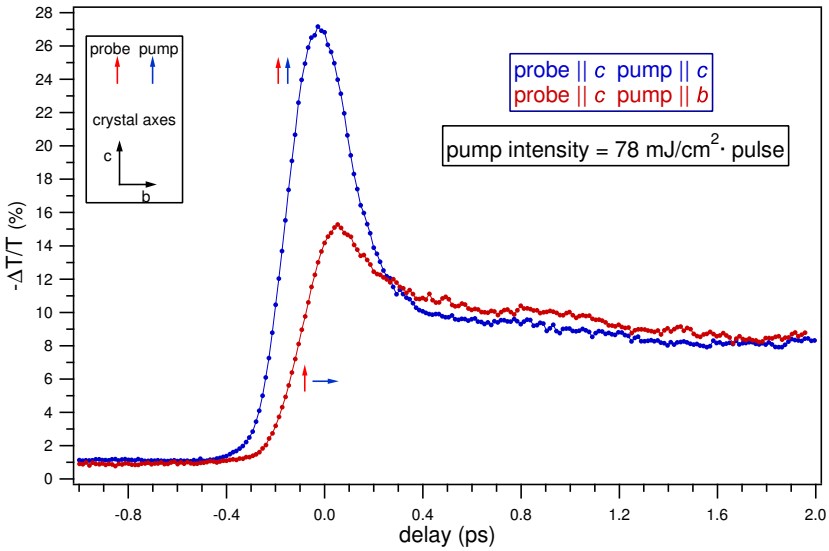


FIGURE 6.5: Investigation of the $CuGeO_3$ absorption of the pump and probe radiation, in the different configurations of polarization with respect to the crystal axes (pump-probe//$c$; probe//$c$ pump//$b$). The incident intensity of the pump beam is held constant.

sented in Fig. 6.5 and 6.6.

In Fig. 6.5, the first measurement is carried out with both pump and probe polarized parallel to the $c$ axis of the crystal (probe//$c$ pump//$c$ - blue marks), i.e. the same configuration of the previous measurements. The measured dynamics is in agreement with the results reported in Fig. 6.4. Now it is interesting to analyze what happens when we vary the axes of polarization of the pump beam. If we rotate the pump polarization to be parallel to the crystal $b$ axis, with the probe still aligned along $c$ (probe//$c$ pump//$b$ - red marks), the fast absorption peak is reduced to about one half with respect to the previous configuration, but the relaxation tail remains about the same. This result indicates that, while the fast dynamics is strongly dependent on the excitation polarization, the signal variation detected after about 1 ps is not subjected to any selection rule and is related only to the total incident power. This can be interpreted by looking at the optical absorption properties of $CuGeO_3$ reported in Fig. 3.1 of Chapter 3. The light

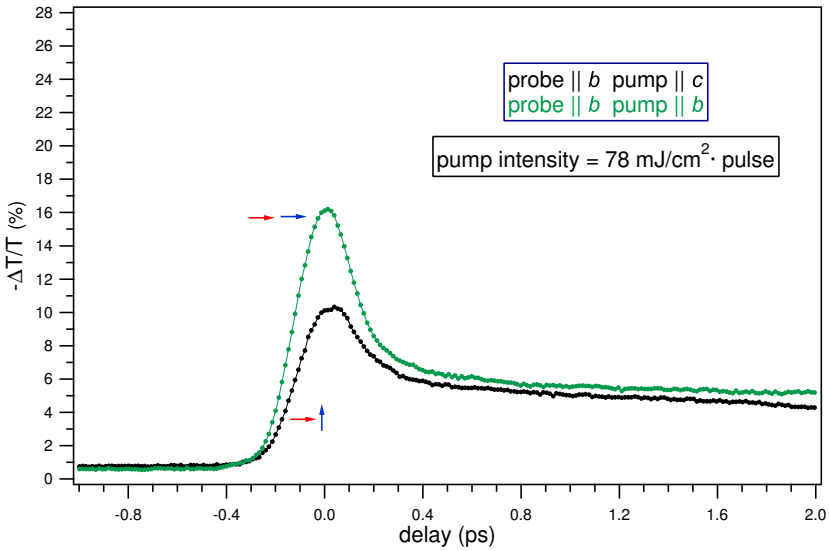


FIGURE 6.6: Investigation of the $CuGeO_3$ absorption of the pump and probe radiation, in the different configurations of polarization with respect to the crystal axes (pump-probe//$c$; probe//$c$ pump//$b$; pump-probe//$b$). The incident intensities are held constant.

absorption at $h\nu$=3.14 eV can be primarily attributed to the Zhang-Rice singlet excitation, but a role is played also by the tail of the direct charge-transfer edge, as evident from the residual absorption when the $h\nu$=3.14 eV polarization is set parallel to the $b$-axis and the Zhang-Rice singlet excitation is suppressed. As a consequence, we can state that the fast dynamics, related to a modification of $d$-$d$ transitions, varies when a high-density of Zhang-Rice excitons is created, whereas the slower dynamics is only related to the $O_{2p} \rightarrow Cu_{3d}$ charge-transfer process.

In Fig. 6.6, the results obtained by changing the probe polarization are shown. It is evident that the transmittivity variation signal is lowered when the probe polarization is along the $b$-axis. This finding can be attributed to the difference of the optical properties of $CuGeO_3$ upon changing the IR light polarization, as shown in Fig. 3.1. In the configuration probe//$b$ pump//$b$ (Fig. 6.6 - green marks) the relaxation of the signal is similar to the results obtained for the probe//$c$ configuration, reported in Fig. 6.5, where a fast and a slow dynamics can be

recognized.

If the pump is turned in the $c$-alignment, in order to excite the Zhang-Rice singlets (probe//$b$ pump//$c$ - black marks), the fast absorption peak is lowered, while the slow dynamics is substantially unchanged. The independence of the slow signal on the pump polarization further confirms the attribution to the direct charge-transfer process, as previously discussed. On the contrary, the fast signal behavior is opposite with respects to the results obtained for the probe//$c$ configuration. A detailed investigation of the physical origin of the probe transmittivity variation is needed in order to understand in detail the interplay between the Zhang-Rice excitons formation and the fast dynamics of the IR optical properties.

### 6.2.3 Pump fluence dependence of transmittivity variation

For each of the above configurations we perform a series of measurements varying the pump incident power. The photon density varies between $0.2{\cdot}10^{20}$ cm$^{-3}$ and $2{\cdot}10^{20}$ cm$^{-3}$, i.e. the photodoping ranges between 0.2% and 2%. Above the threshold of about $2{\cdot}10^{20}$ photons/cm$^3$ the $CuGeO_3$ crystal is damaged and reversible measurements can be no longer obtained. This means that the measured variation of the transmittivity of the order of tens of percentage is the consequence of a very strong perturbation of the system, near the irreversible collapse of the electronic and crystal structure.

The results of the pump-intensity dependence are shown in Fig. 6.7 and 6.9. Once more $\Delta T/T$ is plotted against the time delay between the pump and probe pulses and it is negative. In each graph are reported the measurements in the same configuration of pump and probe polarizations, where only the pump incident power is changed. The transmittivity variation well follows the previous results of the polarization dependence investigation, with a fast and a slow dynamics in the picosecond timescale. For the series in the configuration with the pump

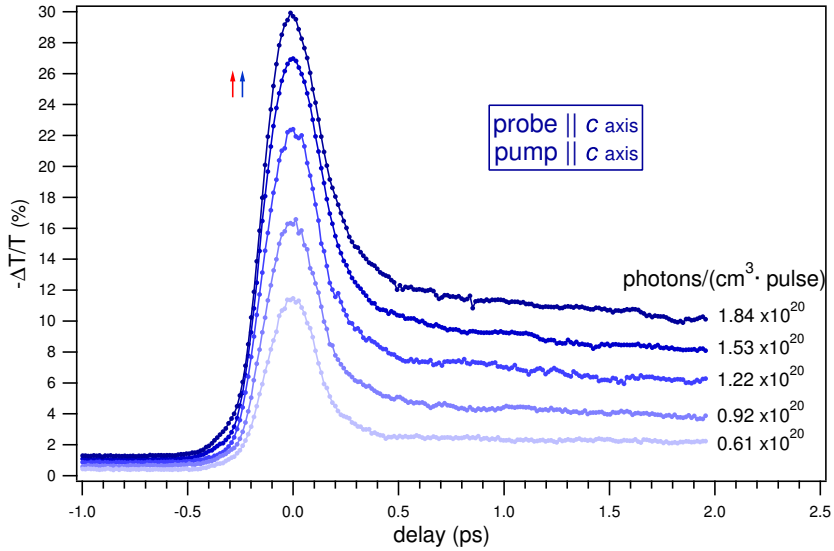


FIGURE 6.7: Time-resolved transmittivity variation measurements, varying the pump incident intensity. The pump and probe are polarized along the crystal $c$ axis.

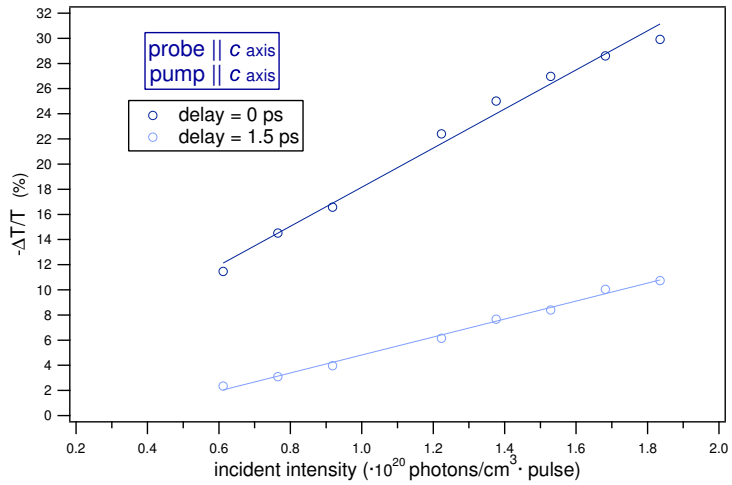


FIGURE 6.8: $CuGeO_3$ absorption versus incident pump intensity, at different time delays. The pump and probe are polarized along the crystal $c$ axis.

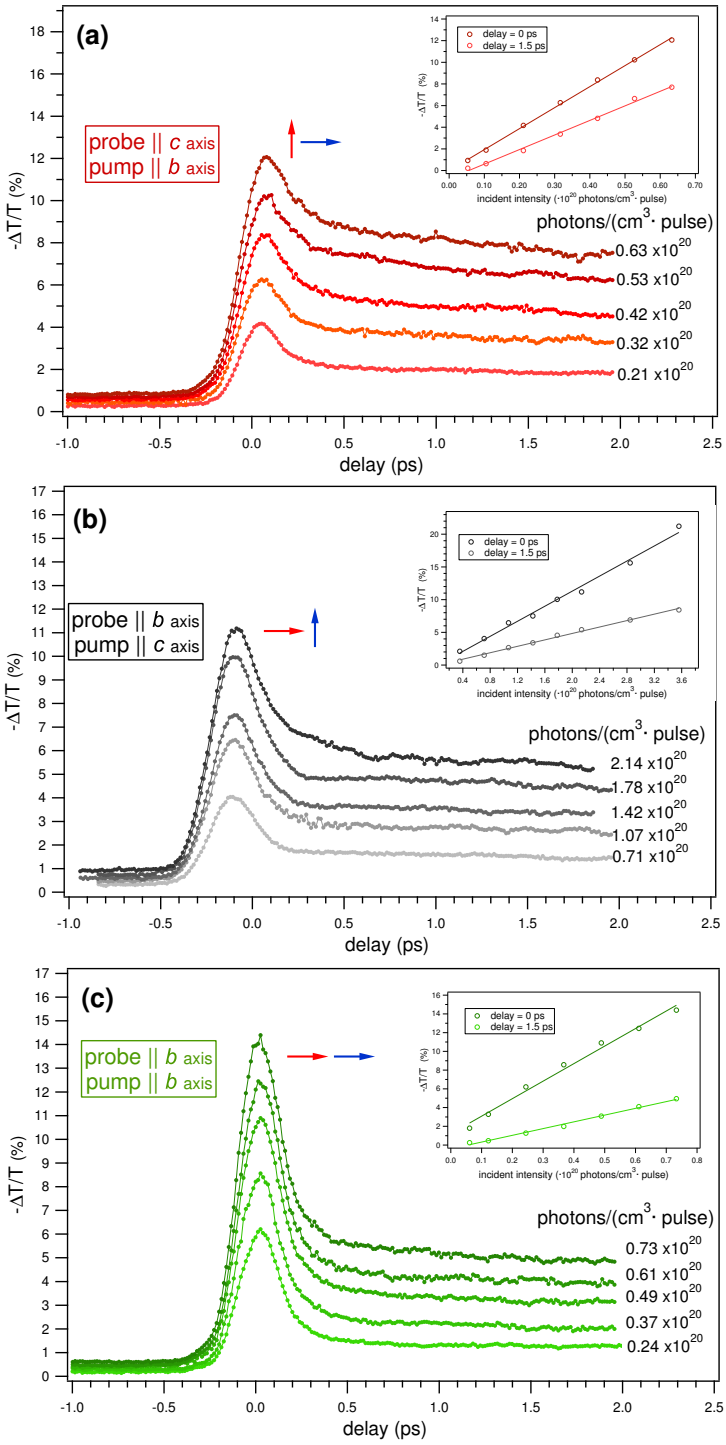


FIGURE 6.9: Time-resolved transmittivity variation measurements, varying the pump incident intensity. (a) probe//$c$ pump//$b$. (b) probe//$b$ pump//$c$. (c) probe//$b$ pump//$b$. In the inlays, the linearity of $CuGeO_3$ absorption versus the incident pump intensity is reported, for different time delays (0 ps and 1.5 ps).

and probe radiation polarized along the crystal $c$ axis, we report in Fig. 6.8 the values of $\Delta T/T$ values at two different time delays (0 ps and 1.5 ps). The data are fitted with a linear function (solid lines in Fig. 6.8), demonstrating that the absorption variation increases linearly with the pump incident radiation up to the damage threshold. This linear trend excludes any role played by the non-linear absorption (2nd order) of the pump radiation previously observed (Sec. 6.1), which would result in a transmittivity variation quadratic in the pump intensity. These results are confirmed in the other three series for the different configurations of polarization (insets in Fig. 6.9). As a consequence, the perturbation of the optical properties of $CuGeO_3$ in the IR region ($h\nu$=1.57 eV) has to be directly connected to the density of excitation induced by the pump pulse absorption.

### 6.2.4 Pump fluence dependence of relaxation dynamics

In this section we report and discuss the relaxation dynamics as a function of the pump intensity. The fit to short-range ($0< \Delta t<2$ ps) and long-range ($\Delta t<15$ ps) time-resolved transmittivity variation measurements are performed with, a double and a triple exponential decay respectively, convoluted with a gaussian function representing the experimental time resolution. Both the pump and probe beams are polarized along the $c$ axis. The data and the fits are reported in Fig. 6.10 and 6.11.

In the inset of Fig. 6.10 the values of the fast decay time-constant $\tau_1$ are reported as a function of the pump intensity. The $\tau_1$ value increases with the incident intensity, indicating a dependence of the fast relaxation dynamics on the Zhang-Rice excitons density. On the contrary the $\tau_2$ and $\tau_3$ behavior, reported in the inset of Fig. 6.11, as a function of the pump intensity is more complex. In particular they are approximately constant up to a threshold value for the excitation intensity of about $1.5 \cdot 10^{20}$ photons/cm$^3$. Above this threshold the long-

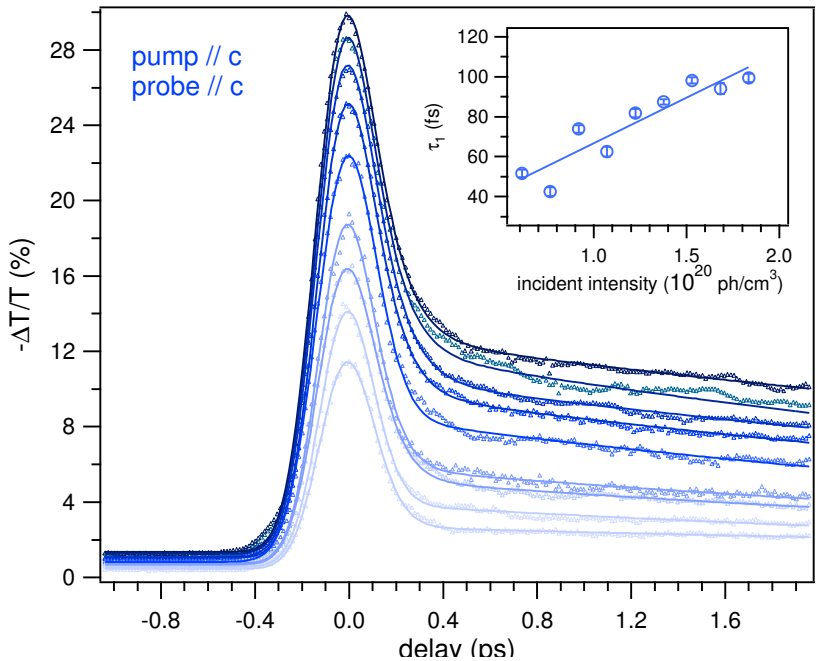


FIGURE 6.10: Short range time-resolved transmittivity variation measurements, with different pump incident intensities in the probe//$c$ pump//$c$ configuration. Solid lines are the fit to the data with a double exponential decay convoluted with a gaussian function. In the inset the value obtained for $\tau_1$ are reported as a function of the photon density of the excitation pulse. The solid line is the linear fit to data.

range dynamics starts to slower before the damage threshold. It is important to note that at low pump intensities ($n_{ph}$ <1.5·10$^{20}$ photons/cm$^3$) the value of $\tau_2$ is very small indicating that the data can be well fitted simply with a double exponential decay. Only at high excitation densities ($n_{ph}$ >1.5·10$^{20}$ photons/cm$^3$) the role of the second exponential decay is evident, as previously noted in section 6.2.1.

The interpretation of these results is very difficult and requires a detailed understanding of the excitation processes. In particular the $\tau_1$ linear increase suggests a dependence of the Zhang-Rice singlets lifetime on the excitation density, whereas the sudden change of the $\tau_2$ and $\tau_3$ values can be interpreted as a different

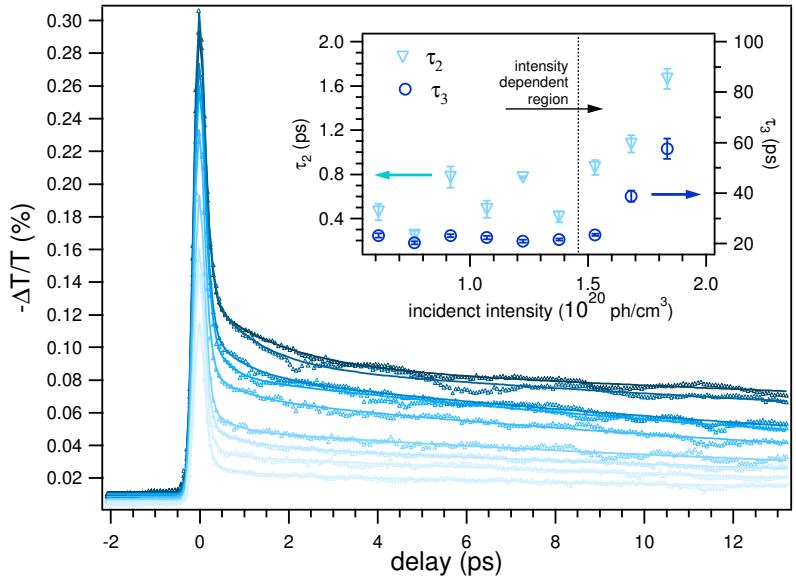


FIGURE 6.11: Long range time-resolved transmittivity variation measurements, with different pump incident intensities in the probe//$c$ pump//$c$ configuration. Solid lines are the fit to the data with a triple exponential decay convoluted with a gaussian function. In the inset the value obtained for $\tau_2$ and $\tau_3$ are reported as a function of the photon density of the excitation pulse.

relaxation regime at very high excitation densities.

## 6.3 Discussion

In the following we will report the most important results obtained from time-resolved transmittivity measurements on $CuGeO_3$ and described in the previous section. As explained before, the sample is excited with UV short pulses ($h\nu$=3.14 eV), in order to photoexcite Zhang-Rice singlets and the direct charge-transfer process between $O_{2p}$ and $Cu_{3d}$ bands. The relaxation dynamics of the photoinduced perturbation is probed in the IR range ($h\nu$=1.57 eV), where the optical properties of $CuGeO_3$ are related to phonon-assisted transitions between the $d$-$d$ Cu levels.

- Upon excitation with high density ($n_{ph}$ $\sim 10^{20}$ photons/(cm$^3$·pulse)) UV radiation, the $CuGeO_3$ single crystal exhibits a huge variation of the optical properties in the IR region. In particular, the measured variation of the IR transmittivity is of the order of tens of percent, whereas the estimated density of the photodoping is about 2%. This result suggests that a deep modification of the properties of the system is induced by the pump excitation.

- Three different relaxation dynamics can be evidenced in the time-resolved signal, by fitting the data with three exponential decays convoluted with a gaussian. The fast dynamics is fitted with a time-constant $\tau_1$ of about 100 fs, which is slightly larger than the pulse time-width. Following the fast relaxation, two exponential decays with time-constants $\tau_2 \simeq 1.5$ ps and $\tau_3 \simeq 50$ ps can be recognized.

- The intensity of the fast dynamics is strongly dependent on the pump polarization. On the contrary the slow dynamics is not influenced by pump polarization, but depends only on the total intensity of the UV radiation impinging on the sample. This results suggest that the fast dynamics is related to a modification of the *d-d* transitions as a consequence of the high density Zhang-Rice singlets excitation, whereas the slower decays are the consequence of the direct charge-transfer process. In particular, the time constant $\tau_3$ can be interpreted as the slow relaxation of the system to the equilibrium conditions before the arrival of the pump pulse.

- The intensity of the transmittivity variation is linear with the pump fluence both in the fast and in the slow regions. This result is the proof that no role is played by non-linear absorption process present at these excitation intensities, as demonstrated by the absorption measurements as a function of the incident intensity, reported in section 6.1. As a consequence the detected transmittivity variation is directly related to the density of photoexcitation

of the system.

- The time-constants of the relaxation dynamics vary with the pump fluence. In particular, the $\tau_1$ value monotonically increase with the intensity of the excitation, whereas $\tau_2$ and $\tau_3$ are about constant for photon densities smaller than $1.5{\cdot}10^{20}$ photons/cm$^3$ and start to increase for greater excitation densities. This result suggests that the lifetime of the Zhang-Rice excitons is linearly dependent on their density, whereas an abrupt change in the relaxation regime for the charge-transfer process takes place at very high excitation densities.

### 6.3.1 Excitation processes

The reported results suggest that while the fast decay is connected to the relaxation of the photoexcited Zhang-Rice singlets, the slower decays are connected to the charge transfer process and the following relaxation on the hundreds of picoseconds time-scale. This allows to conclude that the lifetime of Zhang-Rice excitons is of the order of 100 fs, whereas the lifetime of a $O_{2p}$ hole excited directly through a charge transfer process is about two order of magnitude greater.

The huge difference between the lifetimes of the $O_{2p}$ holes excited via the Zhang-Rice exciton or directly through the charge transfer process between $O_{2p}$ and $Cu_{3d}$ levels can be rationalized in terms of localization on the O site. In fact, as explained in Section 3, the Zhang-Rice exciton is delocalized on the four O atoms surrounding the Cu ion and free to move in the lattice without perturbing the anti-ferromagnetic order [26]. As a consequence, the scattering rate with other electrons photoexcited in the $Cu_{3d}$ bands is very high. On the other side, the charge-transfer process is a local process, where the excited hole in the $O_{2p}$ bands is basically localized in the unit cell and the probability of scattering with electrons photoexcited is strongly reduced.

Unfortunately no lifetime estimations or measurements for this kind of excitons

are available in the literature. A possibility is to compare the measured lifetime with the inverse linewidth of the absorption peak corresponding to the exciton energy, by taking into account the relation:

$$\tau = \frac{\hbar}{\gamma} = \frac{658(meV \cdot fs)}{\gamma(meV)} \tag{6.4}$$

Absorption spectra of $CuGeO_3$ in the 15-300K temperature range are reported in Fig. 6.12. To proper evaluate the inverse linewidth we need to avoid contributions from inhomogeneous broadening of the absorption peak. One source is linewidth broadening due to the coupling of the Zhang-Rice excitons with phonons. In particular, the dependence of the broadening of the absorption peak at 1.57 eV on the sample temperature is interpreted as the coupling of the exciton with a longitudinal optical phonon with an energy of about 40 meV [1]. As a consequence, the calculation of the intrinsic linewidth at 300 K ($\gamma \simeq$150 meV) gives an underestimation of the exciton lifetime $\tau \simeq$4 fs. A more realistic estimation can be performed by considering the intrinsic linewidth at measured at 15 K ($\gamma \simeq$50 meV). In this case the lifetime of about 13 fs is closer to the experimental finding but still lower. A probable explanation is related to the fact that the excitonic peak is the consequence of the energy lost during the charge-transfer process and used to create the exciton. As a consequence, the excitonic linewidth depends on the energy spread of the main absorption process. The estimated lifetime of 13 fs has thus to be considered as a lower limit.

Another important result concerns the behavior of the lifetimes $\tau_1$, $\tau_2$ and $\tau_3$ as a function of the excitation intensity. A way towards the understanding of the previously discussed increase of the values of the relaxation time-constant at high pump fluences is to consider in detail the rate equation governing the relaxation process. After the pump excitation, a high concentration $n(t)$ of Zhang-Rice excitons is created. The recombination process can be twofold. A recombination of the exciton with the equilibrium electrons, which gives a term in the rate equation proportional to $-\gamma n(t)$, and a recombination with the excited electrons in the $Cu_{3d}$

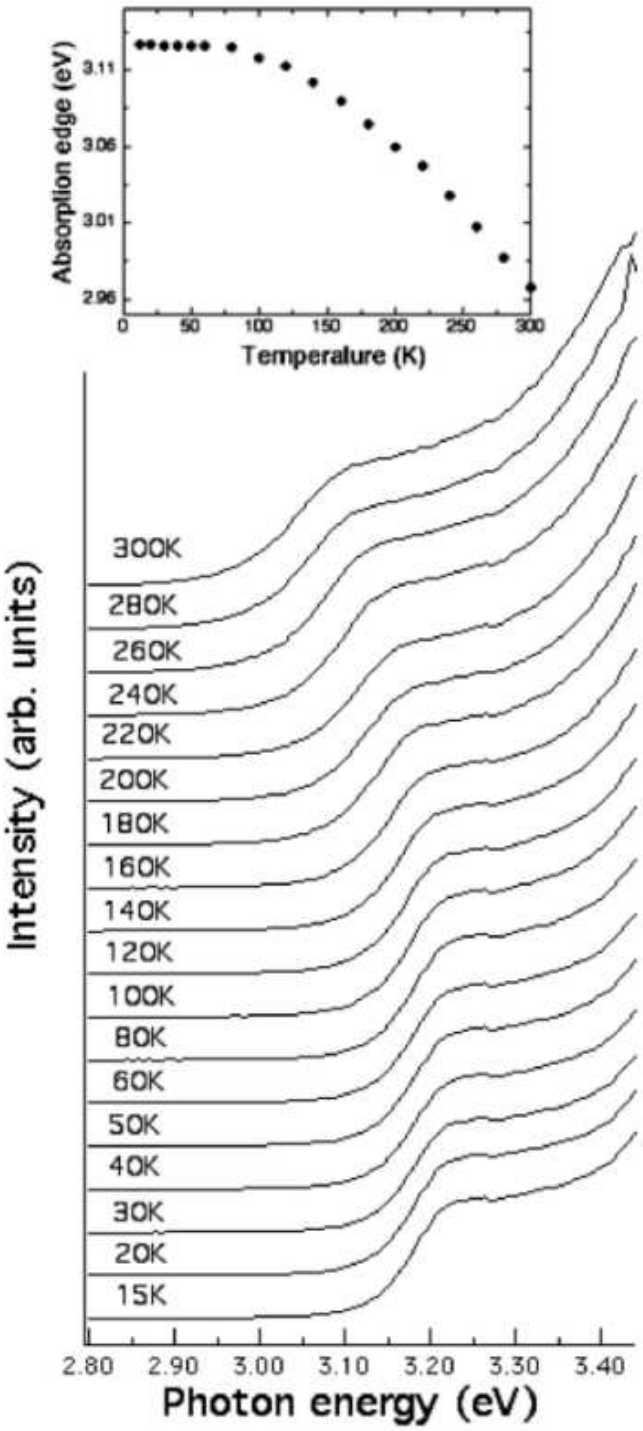


FIGURE 6.12: Absorption spectra of $CuGeO_3$ in the 15-300K temperature range. In the inset the dependence of the Zhang-Rice peak is reported as a function of the temperature. The figure is taken form Ref. [1]

bands, which is responsible for a quadratic term $-\beta n(t)^2$ in the rate equation ($\gamma$ and $\beta$ are the linear and quadratic recombination coefficients, respectively). The rate equation is:

$$\frac{\partial n(t)}{\partial t} = -\gamma n(t) - \beta n(t)^2 \tag{6.5}$$

At low excitation energies the linear term is dominant and the solution of the equation is:

$$n(t) = n(0)e^{-\gamma t} \tag{6.6}$$

where $n(0)$ is the initial density of photoexcited excitons. This is the exponential decay used to fit the experimental data. On the contrary, when the excitation energies increase, the quadratic term dominantes and the solution of the equation is given by:

$$n(t) = \frac{n(0)}{1 + \beta n(0)t} \tag{6.7}$$

which is not an exponential decay, but a power function. As a consequence of the slower decay of a power function with respect to the exponential decay, we can explain why at photon densities grater than $1.5{\cdot}10^{20}$ photons/cm$^3$ we need a three exponential decay to fit the data, whereas at lower excitation intensities the role of the $\tau_2$ decay is reduced and the data can be well fitted with a double decay. These considerations suggest that $n(0) \simeq 1.5{\cdot}10^{20}$ photons/cm$^3$ is the onset of a different decay regime because, at this excitonic density, the recombination process between the Zhang-Rice singlet and the electrons excited in the $Cu_{3d}$ correlated bands dominates.

### 6.3.2 Origin of the modification of the IR absorption

In the previous section we attributed the fast and the slow measured relaxation dynamics of $CuGeO_3$, excited by UV light, to the Zhang-Rice excitons formation and to the direct charge-transfer process, respectively. We now discuss the possible mechanisms responsible for the measured absorption variation.

- **exciton-phonon coupling**

  As discussed in the previous section, the Zhang-Rice excitons are strongly coupled with at least one longitudinal optical phonon with an energy of about 40 meV [1]. This means that the ZR exciton is able to couple with the lattice and induce a deformation in the unit cell. As explained in Chapter 3 the relative energy position of the $d$ levels, splitted as a consequence of the crystal field potential, are strongly dependent on the position of the surrounding O atoms. A possible explanation of the measured variation of the IR transmittivity could be related to a change in the lattice structure induced by the photoexcitation of the Zhang-Rice singlets. A quantitative estimation of this effect needs the evaluation of the splitting of $Cu_{3d}$ levels in a deformed unit cell. However it is possible to rule out this explanation on the basis of timescale considerations. As a matter of fact, the electron-phonon coupling usually acts on the picosecond timescale, whereas a huge transmittivity variation has been detected even in the first hundreds of femtoseconds, where the electronic system is completely decoupled from the lattice. In addition the coherent excitation, through the ZR exciton coupling, of a particular phonon should result in an oscillation in the optical signal with a period of about $\tau = h/E_{phonon} \simeq 1.6$ ps. This kind of oscillation has never been detected during the measurements.

- **opening of new excitation channels**

  The detected transmittivity variation could be attributed to the opening of new excitation channels. In fact the absorption properties of $CuGeO_3$ (see Fig. 3.1 of Chapter 3) refer to the system in the ground state. On the contrary we are probing the IR properties in a high non-equilibrium condition, where about the 2-3% of electrons has been excited to the $Cu_{3d}$ levels. The presence of the photoexcited holes in the $O_{2p}$ bands could open new channels for transitions at the photon energy of 1.57 eV. One possible transition in the IR range could regard a change in the $O_{2p}$ symmetry with-

out any further charge transfer, i.e an excitation of the hole to one of the splitted levels of the configuration $3d^{10}\underline{L}$ (see Fig. 3.4 of Chapter 3). Another possible mechanism involves the filling of the $O_{2p}$ holes by electrons from the Ge bands. A quantitative estimation of these possible transitions needs the detailed knowledge of the complete $CuGeO_3$ band structure. This explanation is compatible with the measured fast dynamics of the order of hundreds of femtosecond but should result in a variation of the optical properties of a fraction of the photoinduced Zhang-Rice excitons density. On the contrary, after excitation of about 3% of Zhang-Rice singlets, the measured transmittivity variation is as high as 30%.

- **band-gap collapse**

  The most interesting explanation of the experimental results concerns the possibility of a very fast collapse of the band gap as a consequence of the high-density excitation. In particular, as explained in Chapter 2, the band gap is originated from the strong correlations of electrons in the $Cu_{3d}$ bands. The Coulomb repulsion prevents electrons from hopping from one site to the neighbor one and the conductivity, predicted by the independent-electron approximation, is suppressed. As a consequence, the photoinduced modification of the correlated $3d$-bands occupation could induce a dramatic modification of the electron correlations resulting in a collapse of the band-gap. This explanation is compatible both with the velocity of the measured fast decay ($\sim$100 fs) and with the huge intensity of the transmittivity variation signal ($\Delta T/T \sim 20\%$). This kind of effect has been already proposed to interpret time-resolved reflectivity measurements on a strongly correlated system [30] and constitutes a very interesting issue in the study of the electronic properties of these peculiar materials.

# Chapter 7

# Conclusions

In conclusion we have investigated the strong correlated system $CuGeO_3$ through time-resolved optical spectroscopy. In particular we studied the effects of the high-density photoexcitation of the Zhang-Rice singlets in the sample, on the absorption dynamics in the *d-d* transitions energy region at 1.57 eV. The main results are:

Upon excitation with high density ($n_{ph}$ $\sim 10^{20}$ photons/(cm$^3$·pulse)) UV radiation, the $CuGeO_3$ single crystal exhibits a huge variation (up to 30%) of the optical properties in the IR region. This finding could be attributed to the collapse of the charge-transfer gap as a consequence of the photoinduced perturbation of the strongly correlated $Cu_{3d}$ bands.

Different relaxation dynamics are evidenced in the time-resolved signal: a fast decay with a time-constant $\tau_1$ of about 100 fs, which is slightly larger than the pulse time-width and, following the fast relaxation, an exponential decay with a time-constant of about 50 ps can be recognized. At excitation densities greater than $1.5 \cdot 10^{20}$ photons/cm$^3$ the relaxation dynamics can no longer be described by a double exponential decay. This result suggests a role played by the recombination of the photoexcited holes in the $O_{2p}$ bands with the electrons excited in the $Cu_{3d}$ bands.

The intensity of the fast dynamics is strongly dependent on the pump polar-

ization. This allows to disentangle the contribution to the signal of the Zhang-Rice excitons formation and of the direct charge-transfer process.

The intensity of the transmittivity variation is linear with the pump fluence both in the fast and in the slow regions. This result is the proof that no role is played by non-linear absorption processes present at these excitation intensities.

# Bibliography


[1] S. Pagliara, F. Parmigiani, P. Galinetto, A. Revcolevschi, and G. Samoggia, Phys. Rev. B **66**, 024518 (2002).

[2] M. Bassi, P. Camagni, R. Rolli, G. Samoggia, F. Parmigiani, G. Dhalenne, and A. Revcolevschi, Phys. Rev. B **54**, 11030 (1996).

[3] C. de Graaf and R. Broer, Phys. Rev. B **62**, 702 (2000).

[4] S. Pagliara, Ph.D thesis, Universitá degli studi di Brescia, 1999.

[5] J. B. Goodenough, Phys. Rev. **100**, 564 (1955).

[6] J. Kanamori, J. Phys. Chem. Solids **10**, 87 (1959).

[7] P. W. Anderson, Solid State Phys. **14**, 99 (1963).

[8] N. F. Mott, *Metal Insulator Transitions* (Taylor and Francis, London, 1990).

[9] J. Hubbard, Proc. Roy. Soc. London A **276**, 238 (1963).

[10] A. Damascelli, Z. Hussain, and Z.-X. Shen, Rev. Mod. Phys. **75**, 473 (2003).

[11] J. Zaanen, G. A. Sawatzky, and J. W. Allen, Phys. Rev. Lett. **55**, 418 (1985).

[12] M. Hase, I. Terasaki, and K. Uchinokura, Phys. Rev. Lett. **70**, 3651 (1993).

[13] N. Tsuda, K. Nasu, A. Fujimori, and K. Siratori, *Electronic Conduction in Oxides* (Springer, Berlin, 2000).

[14] S. L. Altmann, *Band Theory of Solids. An Introduction from the Point of View of Simmetry* (Clarendon Press, Oxford, 1994).

[15] M. Hase, I. Terasaki, K. Uchinokura, M. Tokunaga, N. Miura, , and H. Obara, Phys. Rev. B **48**, 9616 (1993).

[16] P. H. M. van Loosdrecht, S. Huant, G. Martinez, G. Dhalenne, and A. Revcolevschi, Phys. Rev. Lett. **76**, 311 (1996).

[17] P. H. M. van Loosdrecht, S. Huant, G. Martinez, G. Dhalenne, and A. Revcolevschi, Phys. Rev. B **54**, 3730 (1996).

[18] P. H. M. van Loosdrecht, J. Zeman, G. Martinez, G. Dhalenne, and A. Revcolevschi, Phys. Rev. Lett. **78**, 487 (1997).

[19] A. Damascelli, D. van der Marel, F. Parmigiani, G. Dhalenne, and A. Revcolevschi, Phys. Rev. B **56**, 11373 (1997).

[20] V. Corradini, A. Goldoni, F. Parmigiani, C. Kim, A. Revcolevschi, L. Sangaletti, and U. del Pennino, Surf. Sci. **420**, 142 (1999).

[21] H. Eskes, L. H. Tjeng, and G. Sawatzky, Phys. Rev. B **41**, 288 (1990).

[22] H. Kuzmany, *Solid-State Spectroscopy* (Springer, Berlin, 1998).

[23] N. Ashcroft and N. Mermin, *Solid State Physics* (Holt, Rinehart and Winston, New York, 1976).

[24] C. M. Wolfe, N. Holonyak, and G. E. Stillman, *Physical Properties of Semiconductors* (Prentice Hall, New Jersey, 1989).

[25] R. A. Kaindl, M. A. Carnahan, D. Hägele, R. Lövenich, and S. Chemla, Nature **423**, 734 (2003).

[26] F. C. Zhang and T. M. Rice, Phys. Rev. B **37**, 3759 (1988).

[27] P. W. Anderson, Science **235**, 1196 (1987).

[28] Technical Note TN 1000, Technical Note TN 1001 and Application Note AN 1003, Ametek Signal Recovery.

[29] A. Revcolevschi and G. Dhalenne, Adv. Mater. **5**, 657 (1993).

[30] T. Tonogai, T. Satoh, K. Miyano, Y. Tomioka, and Y. Tokura, Phys. Rev. B **62**, 13903 (2000).

# Acknowledgements

I conclude this thesis with a few acknowledgements. I am grateful to Prof. Gabriele Ferrini, who accepted to be the supervisor of this thesis and who made this work possible. I thank him for his help, the discussions and suggestings.
A huge thanks goes to Claudio Giannetti, a great scientific guide for me and a friend before all. He is the one giving a sense to everything I doubt about.
I thank all the people who gave me an help in this work, from the measurements in the lab to the writing of the paper. I acknowledge Stefania Pagliara, for the important suggestings and for the help in the calculations, Gianluca Galimberti and Emanuele Pedersoli, a great lab fellow.
I also acknowledge Prof. Fulvio Parmigiani for reviewing the paper and who also made this work possible.
I finally want to thank all the people who gave a scientific support to me and Claudio with their experience and interests in the subject.

Preferisco ringraziare in questo modo le persone care, gli amici di sempre e i compagni in questa esperienza.
Alla mia famiglia devo piú di ogni altra cosa. A Pietro, Graziella, Ermanno e Cecilia grazie per essermi stati cosí vicino e avermi aiutato con grossi sacrifici.
Grazie al Prof. Ferrini per avermi aiutato durante tutto questo periodo e insieme al Prof. Parmigiani per aver reso possibile questa tesi di ricerca.
Ringrazio tutti quelli che mi sono stati a fianco in questa esperienza: Claudio perché é grazie a te se a tutto ció ho attribuito a un significato e perché sei insostituibile. Insieme abbiamo scoperto i benefici delle "goleador"! Con Emanuele possiamo sempre dire di essere usciti indenni dal "ristorante Panorama", e non é cosa da poco. Grazie a Stefania e a Gianluca per il vostro aiuto, la prossima volta

ripasseró meglio la soluzione delle equazioni di secondo grado! Grazie a voi tutti perché la gentilezza e la disponibilitá non sono cose da poco.
Ringrazio i compagni di Universitá: é stato bello avere qualcuno con cui condividere gioie, fatiche, critiche e discussioni.
Un grazie vero agli amici di sempre, ai compari di tante avventure. Siete tanti ma nel mio cuore e nei ricordi ci state tutti. Ai compagni di squadra, perché é stata dura ma ce l'abbiamo fatta. Ai compagni di viaggio, perché ne abbiamo combinate tante insieme e abbiamo visto come é fatto il mondo.